



# **Full-wave Characterization of Rough Terrain Surface Effects for Forward-looking Radar Applications: A Scattering and Imaging Study from the Electromagnetic Perspective**

**by DaHan Liao**

**ARL-TR-5758**

**September 2011**

## **NOTICES**

### **Disclaimers**

The findings in this report are not to be construed as an official Department of the Army position unless so designated by other authorized documents.

Citation of manufacturer's or trade names does not constitute an official endorsement or approval of the use thereof.

Destroy this report when it is no longer needed. Do not return it to the originator.

# **Army Research Laboratory**

Adelphi, MD 20783-1197

---

---

**ARL-TR-5758**

**September 2011**

---

## **Full-wave Characterization of Rough Terrain Surface Effects for Forward-looking Radar Applications: A Scattering and Imaging Study from the Electromagnetic Perspective**

**DaHan Liao**

**Sensors and Electron Devices Directorate, ARL**

REPORT DOCUMENTATION PAGE				Form Approved OMB No. 0704-0188	
<p>Public reporting burden for this collection of information is estimated to average 1 hour per response, including the time for reviewing instructions, searching existing data sources, gathering and maintaining the data needed, and completing and reviewing the collection information. Send comments regarding this burden estimate or any other aspect of this collection of information, including suggestions for reducing the burden, to Department of Defense, Washington Headquarters Services, Directorate for Information Operations and Reports (0704-0188), 1215 Jefferson Davis Highway, Suite 1204, Arlington, VA 22202-4302. Respondents should be aware that notwithstanding any other provision of law, no person shall be subject to any penalty for failing to comply with a collection of information if it does not display a currently valid OMB control number.</p> <p><b>PLEASE DO NOT RETURN YOUR FORM TO THE ABOVE ADDRESS.</b></p>					
1. REPORT DATE (DD-MM-YYYY)		2. REPORT TYPE		3. DATES COVERED (From - To)	
September 2011		Final		2010 to 2011	
4. TITLE AND SUBTITLE  Full-wave Characterization of Rough Terrain Surface Effects for Forward-looking Radar Applications: A Scattering and Imaging Study from the Electromagnetic Perspective				5a. CONTRACT NUMBER	
				5b. GRANT NUMBER	
				5c. PROGRAM ELEMENT NUMBER	
6. AUTHOR(S)  DaHan Liao				5d. PROJECT NUMBER	
				1NE4ii	
				5e. TASK NUMBER	
				5f. WORK UNIT NUMBER	
7. PERFORMING ORGANIZATION NAME(S) AND ADDRESS(ES) U.S. Army Research Laboratory ATTN: RDRL-SER-U 2800 Powder Mill Road Adelphi MD 20783-1197				8. PERFORMING ORGANIZATION REPORT NUMBER  ARL-TR-5758	
9. SPONSORING/MONITORING AGENCY NAME(S) AND ADDRESS(ES)				10. SPONSOR/MONITOR'S ACRONYM(S)	
				11. SPONSOR/MONITOR'S REPORT NUMBER(S)	
12. DISTRIBUTION/AVAILABILITY STATEMENT Approved for public release; distribution unlimited.					
13. SUPPLEMENTARY NOTES					
14. ABSTRACT  In characterizing ground surface clutter as relevant to forward-looking radar applications, a finite-difference time-domain (FDTD)-based solver is proposed to study dielectric surface scattering at low depression angles. The solver's effectiveness and accuracy are carefully evaluated for one-dimensional surfaces by comparing Monte Carlo scattering results to those from a surface integral equation (SIE) approach for various surface parameters and incidence angles. It is demonstrated that satisfactory results can be attained at near-grazing angles for most surface parameters of interest with a relatively small simulation domain size, independent of the incidence angle. Subsequently, FDTD simulations of two-dimensional terrain surfaces are featured, along with a demonstration of the effects of ground clutter on target imaging generated by the time-reversal technique. By providing a practical full-wave simulation framework for the emulation of forward-looking radar operation and imaging, this study is intended to facilitate ongoing investigations into the detectability of discrete ground targets in the presence of distributed variable ground clutter in the near-grazing regime.					
15. SUBJECT TERMS Computational electromagnetic, forward-looking radar, Monte Carlo simulations, rough ground scattering					
16. SECURITY CLASSIFICATION OF:			17. LIMITATION OF ABSTRACT  UU	18. NUMBER OF PAGES  48	19a. NAME OF RESPONSIBLE PERSON
a. REPORT	b. ABSTRACT	c. THIS PAGE			DaHan Liao
Unclassified	Unclassified	Unclassified			19b. TELEPHONE NUMBER (Include area code) (301) 394-1741

---

## Contents

---

<b>List of Figures</b>	<b>iv</b>
<b>1. Introduction</b>	<b>1</b>
<b>2. Validation of FDTD Simulation of Rough Surface Scattering in 2-D</b>	<b>3</b>
2.1 SIE Solver.....	4
2.2 FDTD Solver .....	6
2.3 Comparison of SIE and FDTD Results .....	8
<b>3. Extension of FDTD Simulation of Rough Surface Scattering to 3-D</b>	<b>15</b>
<b>4. Emulation of Forward-Looking Radar Imaging in Presence of Ground Clutter</b>	<b>20</b>
4.1 Emulation and Imaging Framework.....	20
4.2 Results and Discussions .....	25
<b>5. Conclusion</b>	<b>31</b>
<b>6. References</b>	<b>33</b>
<b>List of Symbols, Abbreviations, and Acronyms</b>	<b>38</b>
<b>Distribution List</b>	<b>40</b>

---

## List of Figures

---

Figure 1. Electromagnetic wave illuminating a rough surface at grazing angle $\theta_{inc}$ .	2
Figure 2. Description of the FDTD computational domain with a bounded surface perturbation for the rough surface scattering modeling.	7
Figure 3. Errors ( $\Delta$ in dB) in the FDTD-calculated vertical-vertical ( $vv$ )-polarized backscattering coefficient ( $\sigma_{vv}^o$ )—as validated with the SIE solution—at various incidence angles for ground profiles characterized by Gaussian statistics $\{h_{rms}, l_c\}$ ; $\epsilon_r = 5.56$ , $\sigma_d = 10$ mS/m. Annotations at data points are shown, e.g., at $\theta_{inc} = 5^\circ$ , $h_{rms} = 0.3\lambda$ , $l_c = 0.7\lambda$ , $\Delta = 0.40$ dB.	10
Figure 4. Errors ( $\Delta$ in dB) in the FDTD-calculated horizontal-horizontal ( $hh$ )-polarized backscattering coefficient ( $\sigma_{hh}^o$ )—as validated with the SIE solution—at various incidence angles for ground profiles characterized by Gaussian statistics $\{h_{rms}, l_c\}$ ; $\epsilon_r = 5.56$ , $\sigma_d = 10$ mS/m.	11
Figure 5. Comparison of $vv$ -polarized bistatic scattering patterns as derived by SIE (solid lines) and FDTD (dash lines) at various incident angles for two sets of surface parameters: $\{0.1\lambda, 1\lambda\}$ and $\{0.3\lambda, 1\lambda\}$ ; $\epsilon_r = 5.56$ , $\sigma_d = 10$ mS/m.	12
Figure 6. Comparison of $hh$ -polarized bistatic scattering patterns as derived by SIE (solid lines) and FDTD (dash lines) at various incident angles for two sets of surface parameters: $\{0.1\lambda, 1\lambda\}$ and $\{0.3\lambda, 1\lambda\}$ ; $\epsilon_r = 5.56$ , $\sigma_d = 10$ mS/m.	13
Figure 7. Convergence of FDTD solution as function of cell size for surface with parameters $\{0.1\lambda, 1\lambda\}$ ; $\epsilon_r = 5.56$ , $\sigma_d = 10$ mS/m; $\theta_{inc} = 5^\circ$ .	14
Figure 8. Comparison of FDTD-simulated 3-D backscattering results with measured data from reference 9: $h_{rms} = 4$ mm, $l_c = 8.4$ cm, $\epsilon_r = 15.57$ , and $\sigma_d = 0.31$ S/m. At angles close to normal ( $\theta_{inc} \rightarrow 90^\circ$ ), the strong measured response is due to the inclusion of a coherent surface reflection component; this component is not modeled in the simulations.	17
Figure 9. Comparison of FDTD-simulated 3-D backscattering results with measured data from reference 9: $h_{rms} = 3$ cm, $l_c = 8.8$ cm, $\epsilon_r = 8.92$ , and $\sigma_d = 0.19$ S/m.	18
Figure 10. Angular and spectral distribution of backscattering from a rough surface with surface parameters $h_{rms} = 1$ cm, $l_c = 7$ cm, $\epsilon_r = 5.56$ , and $\sigma_d = 10$ mS/m.	19
Figure 11. Simulated $vv$ -polarized images for $9 \text{ m} \times 19 \text{ m}$ scene: (a) Ground with flat surface; (b) ground with randomly rough surface, $h_{rms} = 1.2$ cm, $l_c = 14.93$ cm; and (c) ground with randomly rough surface, $h_{rms} = 1.6$ cm, $l_c = 14.93$ cm. Ground electrical properties: $\epsilon_r = 8$ , $\sigma_d = 10$ mS/m.	22
Figure 12. Simulated $hh$ -polarized images for $9 \text{ m} \times 19 \text{ m}$ scene: (a) Ground with flat surface; (b) ground with randomly rough surface, $h_{rms} = 1.2$ cm, $l_c = 14.93$ cm; and (c) ground with randomly rough surface, $h_{rms} = 1.6$ cm, $l_c = 14.93$ cm. Ground electrical properties: $\epsilon_r = 8$ , $\sigma_d = 10$ mS/m.	23

Figure 13. Simulated  $h\nu$ -polarized images for  $9\text{ m} \times 19\text{ m}$  scene: (a) Ground with flat surface; (b) ground with randomly rough surface,  $h_{rm} = 1.2\text{ cm}$ ,  $l_c = 14.93\text{ cm}$ ; and (c) ground with randomly rough surface,  $h_{rms} = 1.6\text{ cm}$ ,  $l_c = 14.93\text{ cm}$ . Ground electrical properties:  $\epsilon_r = 8$ ,  $\sigma_d = 10\text{ mS/m}$ . .....24

Figure 14. Probability density of  $\nu\nu$ -polarized ground response: histogram shows the distribution inferred from simulated images; solid line is distribution calculated using expression 13. Ground with randomly rough surface: (a)  $h_{rms} = 1.2\text{ cm}$ ,  $l_c = 14.93\text{ cm}$ ; (b)  $h_{rms} = 1.6\text{ cm}$ ,  $l_c = 14.93\text{ cm}$ ; (c)  $h_{rms} = 2.0\text{ cm}$ ,  $l_c = 14.93\text{ cm}$ ; and (d)  $h_{rms} = 2.4\text{ cm}$ ,  $l_c = 14.93\text{ cm}$ . Ground electrical properties:  $\epsilon_r = 8$ ,  $\sigma_d = 10\text{ mS/m}$ . .....30

INTENTIONALLY LEFT BLANK.



---

## 1. Introduction

---

The detection and identification of landmines and unexploded ordnance (UXO) is a difficult problem that has continuously challenged our military's scientific and technological expertise. Of the various mitigation efforts the U.S. Army has undertaken over the years in response to these threats, sensing with radio waves has garnered significant attention—and also has gradually become the most prominent technique. In this method, a transmitter illuminates a scene with electromagnetic signals and then the reflected—or scattered—signals are recorded and processed to identify the presence and locations of potential targets. As a target's signature is often distorted or obscured by the responses from the environment, the ability to model and simulate the target's electromagnetic interactions with its surroundings is therefore critical in the development of high fidelity detection systems.

An important sub-problem in electromagnetic-oriented sensing of both surface and underground targets is the evaluation and understanding of ground surface scattering behavior. Although many phenomenological studies for natural surfaces have been carried out within the radio frequency (RF) remote sensing community on the inference of physical parameters (such as soil composition and moisture content) from the surfaces' polarimetric and spectral scattering signature, the emphasis of contemporary investigations has been primarily on applications related to airborne or spaceborne technologies. As such, the standard radar operational modality of interest is often confined to non-grazing observation angles while the operational frequency is at  $L$ -band and above. Recently, there has been considerable interest in the development of ground-based mobile sensing platforms for standoff detection and identification of in-road and roadside threats (*I-4*). In these low-to-ground systems, as the radio wave propagation paths defining the electromagnetic interactions between the radar transceiver and targets adhere to the ground, existing ground surface scattering models must be supplemented, or extended, to include low grazing angle effects. Accordingly, a full-wave electromagnetic simulation approach is proposed in this work to estimate rough surface background clutter as relevant to performance prediction for the forward-looking imaging radar developed at the U.S. Army Research Laboratory (ARL).

The low-frequency, ultra-wideband, synchronous impulse reconstruction (SIRE) radar testbed (*I*) designed by ARL is a vehicle-based system operating at the nominal frequency band of 500–2500 MHz with the forward-looking coverage angle  $\theta_{inc}$  (figure 1) spanning approximately  $5^\circ$ – $15^\circ$  with respect to the horizon. Although the performance of the radar can be limited by either the “target-to-system noise” or the “target-to-background” ratio, the subject of interest in the current study is the latter quantity as it directly defines the theoretical physics-based detectability limits of the radar. A salient feature associated with scattering from surface targets at grazing angles is that the signal illuminating the target, as well as the signal subsequently re-

radiated by the target, both experience substantial attenuations owing to the near cancellation of their direct and ground-reflected wavefronts. As a result, the backscattered signal from the ground itself may turn out to be strong enough to act as an interference component in masking the target response. Explicitly, it is the relative strength of these two signals that needs to be carefully studied, especially for a small discrete target.

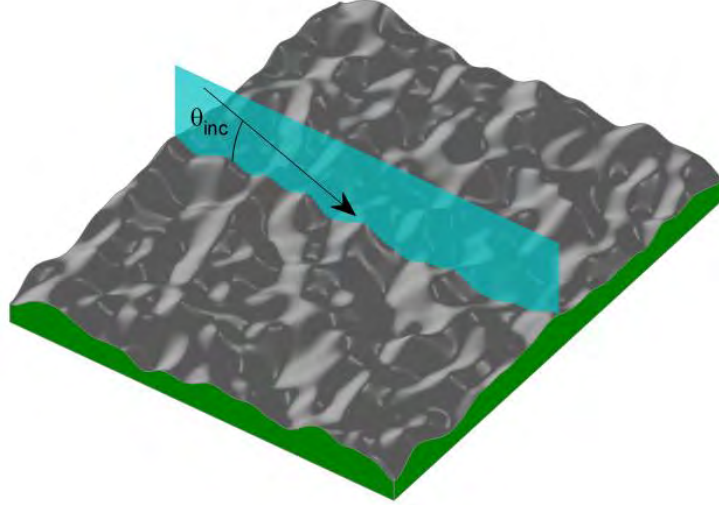


Figure 1. Electromagnetic wave illuminating a rough surface at grazing angle  $\theta_{inc}$ .

The strength and pattern of the backscattered signal from the ground are complicated functions of the radar geometry (i.e., signal incidence and observation angles), transmission and reception polarizations, frequency, as well as the electrical and physical properties of the ground. The unique properties, or complications, of near-earth propagation such as surface wave propagation, non-plane wave propagation, and higher order reflection and diffraction phenomena pose additional constraints that often beset the validity of classical analytical ray-tracing and physical optics techniques—and their heuristic extensions. Another issue in need of further investigation is how these special grazing effects can be exploited for target signature extraction and image clutter suppression pertaining to radar applications. Alas, few comprehensive experimental data sets exist for characterizing ground clutter at the frequency band stated earlier. In open literature, for example, area-wide land clutter data can be found in references 5 and 6 at five frequency bands (very high frequency [VHF], ultra high frequency [UHF], and  $L$ -,  $S$ -, and  $X$ -bands), but these data are only relevant for a radar with a field of view spanning over many kilometers of terrain. The empirically based formula presented in reference 7 (derived from measurements in reference 8) for estimating background clutter is only valid at the higher frequency bands. Fully polarimetric measurements of soil have been done by Oh et al. (9) at  $L$ -,  $C$ -, and  $X$ -bands for a limited set of soil parameters. Overall, there is a scarcity of experimental ground scattering data at grazing angles and low frequencies.

Theoretical studies of scattering and propagation in the presence of an undulating interface separating two media (e.g., air/ground) have been undertaken by various researchers. Commonly employed analytical approaches for computing electromagnetic surface scattering include the small perturbation method (SPM) (10) and the Kirchhoff approximation (KA) (11, 12). The validity of these theoretical techniques is dependent upon the physical statistics of the surface profile. Specifically, SPM is only applicable for surfaces with root mean square (*rms*) height variations much smaller than the wavelength, whereas KA is intended for surfaces with undulations that are large compared to the wavelength (as long as the average radius of curvature of the profile is also large). In addition, these methods do not produce meaningful results when applied to modeling scattering and propagation phenomena at near-grazing angles. Over the years, much effort has been devoted to supplementing perturbation and KA scattering models to extend their range of validity. Works in this endeavor include high-order SPM (13, 14), small slope approximation (15, 16), phase perturbation method (17), unified perturbation expansion (18), and the polarization current-based perturbation expansion (19, 20); however, the emphasis of these studies is not on the grazing configuration. Consequently, closed-form analytical expressions for the radar scattering coefficient derived from the aforementioned techniques may be of limited use for addressing the specific needs of the current problem of interest.

In view of the lack of empirical data and the deficiencies of analytical treatments, numerical simulations of surface scattering effects based on direct field solvers—such as integral equation and finite difference methods—have been put forth in previous works (21) (and references therein). A survey of these studies shows that existing integral equation solvers are rather unattractive for the three-dimensional (3-D) grazing problem and very few of the proposed finite difference methods focus on the grazing scenario at all. The twofold objective of the current study is discussed as follows. First, in sections 2 and 3, the development of the finite-difference time-domain (FDTD) technique based on the finite-extent perturbation surface model is outlined—including a detailed investigation of the validity of the method obtained through comparisons with a high-order surface integral equation (SIE) solution and with published measurement data. Then, in section 4, a demonstration of the effects of ground clutter on target imaging generated by the time-reversal technique is presented with the simulation of a large terrain scene consisting of targets in a rough ground environment. In sum, this study illustrates the practicality of the chosen full-wave simulation strategy for the emulation of forward-looking radar operation and imaging.

---

## 2. Validation of FDTD Simulation of Rough Surface Scattering in 2-D

---

The purpose of this section is to determine the accuracy (and limitations) of the proposed FDTD algorithm for various grazing incidence angles and terrain surface parameters by using a high-order SIE-derived solution as the reference solution. Motivations are also given to illustrate why

the employed approach may be more appropriate than the SIE solver for the current work of interest. To this end, the SIE solver is discussed first, followed by the FDTD. The two-dimensional (2-D) problem is considered at the moment to reduce the computational complexity of the validation process.

## 2.1 SIE Solver

The high-order accurate integral equation solver originally developed in references 22 and 23 for long-distance, near-ground wave propagation applications is modified to characterize scattering from an irregular terrain profile. The solver discretizes the Poggio, Miller, Chang, Harrington, Wu, and Tsai (PMCHWT) (24–26) combined-field surface integral formulation using the regular locally corrected Nyström (LCN) method (27). In essence, the following boundary conditions are observed at the one-dimensional (1-D) ground surface in relating the incident electric and magnetic fields to the induced electric and magnetic surface currents:

$$\begin{aligned}\hat{n} \times \vec{E}_{inc} &= -\hat{n} \times [(\eta_1 \mathbf{L}_1 + \eta_2 \mathbf{L}_2) \vec{J}(t) - (\mathbf{T}_1 + \mathbf{T}_2) \vec{M}(t)]; \\ \hat{n} \times \vec{H}_{inc} &= -\hat{n} \times [(\mathbf{T}_1 + \mathbf{T}_2) \vec{J}(t) + (\eta_1^{-1} \mathbf{L}_1 + \eta_2^{-1} \mathbf{L}_2) \vec{M}(t)];\end{aligned}\tag{1}$$

where  $\hat{n}$  is the surface normal vector,  $\eta_{v=1,2}$  the medium impedance, and  $\mathbf{L}_v$  and  $\mathbf{T}_v$  the linear integral operators defined in reference 23. It should be noted that the kernels of these operators are first regularized as necessary before the application of the quadrature-based scheme. Then, the interpolated surface profile is divided into equilength segments of length  $h$  with  $N_q$  quadrature points distributed on each segment, and equation 1 is transformed into a matrix system with Gauss-Legendre quadrature as the underlying quadrature rule of the LCN method. In the present formulation, the far-field component of the impedance matrix is extracted and then is characterized by a standard two-level fast multipole method (FMM) of  $O(N^{1.5})$  complexity in memory and central processing unit (CPU) load. Intermediate-distant interactions are accounted for by single-point evaluations of the kernels in equation 1. Near (or local) field interactions are provided by the corrected quadrature weights derived from testing the regularized kernels with Legendre polynomials of orders  $n = 0, 1, 2, \dots, N_q - 1$ . The overall algorithm achieves controllable exponential error convergence of the form  $O(h^{N_q})$ ; consequently, fewer number of unknowns are needed to attain the solution—at a given level of accuracy—as compared to conventional low-order method of moments (MoM) schemes.

In the outlined integral equation approach, the physical surface must be truncated into a finite simulation domain. For the radar scattering problem, mechanisms must be build into the solver in order to sufficiently suppress the surface end effects. This is especially critical for the calculation of the signal in the backscattering directions, where the surface scattering components can be much weaker than the edge diffracted waves. In this study, the following tapered beam (28) is applied as the excitation:

$$\vec{u}_{inc} = \vec{u}_o e^{-j\vec{k}_{o,inc} \cdot \vec{r}(1+w)} e^{-\frac{(x+y \cot \theta_{inc})^2}{g^2}}; \quad (2)$$

where  $\vec{u}_{inc} = \vec{E}_{inc}, \vec{H}_{inc}$  and

$$\vec{k}_{o,inc} = k_o (\hat{x} \cos \theta_{inc} - \hat{y} \sin \theta_{inc}); \quad (3)$$

$$w = \frac{\left[ \frac{2(x+y \cot \theta_{inc})^2}{g^2} - 1 \right]}{(k_o g \sin \theta_{inc})^2}, \quad (4)$$

in which  $g$  is a parameter controlling the beamwidth of the illumination. As equation 2 is essentially only a closed-form approximation to the superposition of a continuous spectrum of Gaussian-weighted plane waves, it does not satisfy the wave equation exactly—that is, it is not Maxwellian in nature. In fact, for fixed  $g$ , the resultant error in the scattering solution grows with decreasing incident angle. It has been shown (28) that in order to consistently achieve accurate solutions, the parameter  $g$  should adhere to the criterion

$$g \gg \frac{1}{k_o \sin \theta_{inc}}. \quad (5)$$

A more substantive definition for  $g$  (or, specifically, its minimum) has been derived by Ye and Jin (29)—and is followed by the present work:

$$g_{min} = \frac{6\lambda}{(\sin \theta_{inc})^{1.5}}. \quad (6)$$

After establishing equation 2, the horizontal surface length  $L$  of the simulation domain should be chosen to be large enough to ensure the surface currents near the edges have been sufficiently attenuated. It is seen in this work that the following condition should be met:  $4g < L < 6g$ , where the lower limit is applicable for fast-varying surface profiles and the upper limit for gently varying ones. Because of the requirements imposed on the tapered beam, it is apparent that extremely large simulation domains are needed by the SIE method for characterizing grazing scattering effects. For instance, at  $\theta_{inc} = 5^\circ$ ,  $L \approx 1400\lambda$ . Simulations of large 1-D surfaces at grazing angles have been carried out previously (30, 31). As an alternative to equation 2, excitation in the form of an integral spectrum of tapered plane waves has been proposed (32, 33). Although such a stimulus is fully Maxwellian, as observed in this work and others (32, 33), a large simulation domain is still necessary for modeling grazing angle phenomena, and therefore, its implementation does not provide a noticeable computational advantage in solving equation 1. A partial explanation to this fact can be reached by noting that, fundamentally, the surface supports a ground wave that is only slightly attenuated by the roughness even though the *rms* slope of the surface variations might be on the order of a wavelength or more (20). Thus, some

energy propagates out to the ends of the surface (and subsequently gets diffracted) even when the ends are not directly illuminated because of the explicit tapering. A complex source beam also has been suggested as an excitation (22), but its use does not seem to provide efficiency improvements in the solver. Instead of manipulating the incident wave, Oh and Sarabandi (34) proposed placing resistive sheets at the ends of a perfectly conducting surface to absorb and minimize the induced edge currents; however, this method has not been verified for dielectric surfaces at grazing angles. (The resistive loading approach has been improved by Zhao and West [35] for extension to surfaces modeled with an impedance boundary condition, but the grazing angle is restricted to be larger than 20°.) A promising technique that avoids the use of both excitation and resistive tapering has been implemented by Spiga et al. The so-called *grazing* MoM approach (36) applies a modified integral equation formulation to a locally perturbed half plane. The computational domain size is shown to be independent of the wave incidence angle.

## 2.2 FDTD Solver

The FDTD method directly solves the differential forms of Maxwell's equations in the spatial and temporal domains. Finite-difference approximations to the curl expressions for the electric and magnetic fields generate the following update equations (for example, for vertical polarization, and assuming isotropic, non-dispersive, non-permeable media):

$$E_x^{n+\frac{1}{2}}\left(i, j+\frac{1}{2}\right)=\frac{\frac{\varepsilon\left(i, j+\frac{1}{2}\right)}{\Delta t}-\frac{\sigma_d\left(i, j+\frac{1}{2}\right)}{2}}{\frac{\varepsilon\left(i, j+\frac{1}{2}\right)}{\Delta t}+\frac{\sigma_d\left(i, j+\frac{1}{2}\right)}{2}} E_x^{n-\frac{1}{2}}\left(i, j+\frac{1}{2}\right) + \frac{1}{\frac{\varepsilon\left(i, j+\frac{1}{2}\right)}{\Delta t}+\frac{\sigma_d\left(i, j+\frac{1}{2}\right)}{2}} \left( \frac{H_z^n(i, j+1)-H_z^n(i, j)}{\Delta y} \right); \quad (7)$$

$$E_y^{n+\frac{1}{2}}\left(i+\frac{1}{2}, j\right)=\frac{\frac{\varepsilon\left(i+\frac{1}{2}, j\right)}{\Delta t}-\frac{\sigma_d\left(i+\frac{1}{2}, j\right)}{2}}{\frac{\varepsilon\left(i+\frac{1}{2}, j\right)}{\Delta t}+\frac{\sigma_d\left(i+\frac{1}{2}, j\right)}{2}} E_y^{n-\frac{1}{2}}\left(i+\frac{1}{2}, j\right) - \frac{1}{\frac{\varepsilon\left(i+\frac{1}{2}, j\right)}{\Delta t}+\frac{\sigma_d\left(i+\frac{1}{2}, j\right)}{2}} \left( \frac{H_z^n(i+1, j)-H_z^n(i, j)}{\Delta x} \right); \quad (8)$$

$$H_z^{n+1}(i, j) = H_z^n(i, j) - \frac{\Delta t}{\mu_o} \left[ \frac{E_y^{n+\frac{1}{2}}\left(i + \frac{1}{2}, j\right) - E_y^{n+\frac{1}{2}}\left(i - \frac{1}{2}, j\right)}{\Delta x} - \frac{E_x^{n+\frac{1}{2}}\left(i, j + \frac{1}{2}\right) - E_x^{n+\frac{1}{2}}\left(i, j - \frac{1}{2}\right)}{\Delta y} \right]. \quad (9)$$

In particular, in this section, the 2-D solver from reference 37 is used as the basis for developing the framework needed for characterizing scattering from the dielectric rough surface. In the approach here, a finite-length rough interface between two media is embedded in an infinite half-space environment (i.e., two dielectric background media separated by a flat plane). The FDTD algorithm implements the split field approach (38), in which the computational domain is partitioned into total and scattered field regions separated by a connective boundary (figure 2). In the absence of any scatterers (i.e., only the half-space background is present in the scene), the scattered field is null everywhere. A scatterer is defined as any perturbation to the half-space configuration (such as a roughness of the interface) and generates non-zero scattered field. In the case of a rough surface, this field represents the incoherent component of the energy scattered by the interface. Note that the incident field is implemented as a uniform plane wave (fully Maxwellian), with the sources at infinity. The incident wavefront is not tapered, but rather a gradual transition from the ends of the rough surface to the infinite flat ground plane is introduced in the interface profile. As such, the support of the scattered field is bounded in the numerical domain, and the method is akin to the aforementioned grazing MoM technique. It is important to emphasize that this bounded surface perturbation approach is different from those of previous FDTD studies on rough surface scattering (39–41) in that only the perturbed (incoherent) field due to the interface roughness is calculated here. In fact, the coherent component of the field reflected by the surface is not included in the solution.

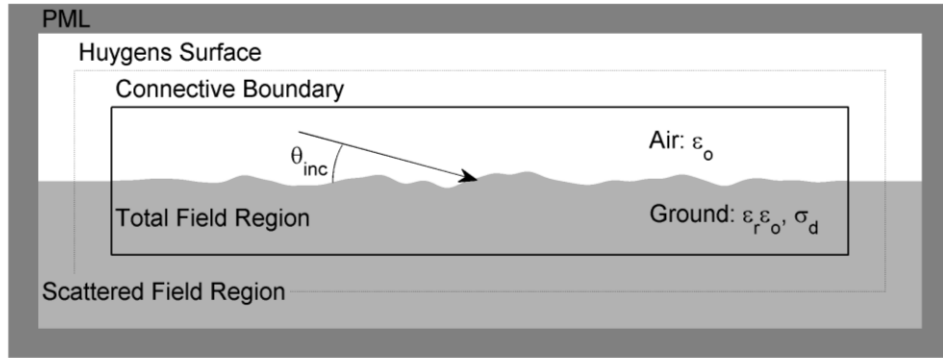


Figure 2. Description of the FDTD computational domain with a bounded surface perturbation for rough surface scattering modeling.

One major issue with the FDTD method is the so-called numerical dispersion (38), which is a result of the finite-difference approximation of the field differential equations. The phase errors introduced by this effect accumulate as the wave propagates through the computational domain and can become significant for large propagation distances. One direct consequence is that in practice, the scattered fields produced by the unperturbed half-space configuration are not exactly null, therefore potentially giving rise to errors that may be comparable in magnitude to the incoherent field scattered by the rough surface. In order to minimize the numerical dispersion artifacts, the unperturbed solution obtained for a flat interface (or the “numerical dispersion error”) is coherently subtracted from the overall solution obtained in the presence of the rough surface.

Throughout this study, the excitation is provided by an unmodulated fourth-order Rayleigh pulse (42). Square Yee cells are used to discretize the entire computational domain; thus, the interface profile is quantized by a stair-stepped approximation. The consequences of this approximation on rough surface modeling are discussed in section 2.3. The horizontal extent  $L$  of the surface is chosen to be 10 times its correlation length—independent of the incidence angle. To emulate an infinite propagation domain, the lattice is surrounded by a perfectly matched layer (PML) on all sides. To compute the far-field scattering pattern, a near-to-far zone transformation is performed with the scattered field sampled at points situated immediately outside the connective boundary (on the closed Huygens surface in figure 2).

As a whole, the technique outlined previously is called here the bounded surface perturbation with coherent error subtraction approach. Its region of validity in terms of the surface parameters and incidence angle is investigated in section 2.3. As opposed to SIE, note the FDTD approach requires a discretization of the entire space enclosed by the domain boundary, and additionally demands the sampling to be compatible with the highest frequency and a domain size compatible with the lowest frequency. Nevertheless, the low implementation complexity and the ability to easily model ground (and target) inhomogeneities—coupled with the fact that the required size of the simulation domain is independent of the incident angle—make the FDTD algorithm a more attractive option for characterizing the grazing scattering behaviors of terrain scenes as needed in this work.

### 2.3 Comparison of SIE and FDTD Results

For communication systems propagation scenarios, the accuracy of the SIE solver has been verified in reference 23. For grazing-angle scattering problems, convergence studies (in terms of  $g$  and  $L$ ) have been carried out within this work to validate the solver’s robustness. Subsequently, as described in this section, efforts are taken to benchmark the accuracy of the proposed FDTD algorithm using the SIE solutions.

In both the SIE and FDTD solvers, the ground is modeled as a homogeneous medium with an effective relative dielectric constant  $\epsilon_r$  and conductivity  $\sigma_d$ . In general, the surface statistics of the ground are described by two functions: the probability density function of the height variations



and the surface autocorrelation function. Within the scope of this study, a zero-mean surface profile  $s(x)$  obeying Gaussian statistics  $\{h_{rms}, l_c\}$ —where  $h_{rms}$  is the *rms* height and  $l_c$  the correlation length—is assumed and generated from its randomized power spectral density function by following the procedure prescribed in reference 28. For the SIE solver, as it is impractical to use  $s(x)$  directly because of the necessity for rapid generation and inter-translation of surface height, length, and slope parameters, an approximate form for  $s(x)$ , which facilitates efficient computation of these routines, must be employed. Therefore, an approximate  $s(x)$  is reconstructed from a sampled set of  $s(x)$  using the approximate prolate spheroidal wave function (APSWF) (43) as the basis. Although only surfaces with Gaussian statistics are considered in this work, the tools described are flexible enough to allow the generation and analysis of arbitrary band-limited roughness profiles.

In interpreting the simulated responses, the radar parameter of interest is the incoherent scattering coefficient of the surface, which is approximated here as

$$\sigma^o = \lim_{r \rightarrow \infty} \frac{r \left\langle \left| \vec{u}_{scat}(\theta_s) - \langle \vec{u}_{scat}(\theta_s) \rangle \right|^2 \right\rangle}{|\vec{u}_{inc}|^2 L_{illu}}; \quad (10)$$

for the FDTD solver,  $L_{illu}$ , the effective length of the surface illuminated by the incident field, is the entire length of the surface perturbation, whereas, for the SIE solver,  $L_{illu} = g(\pi/2)^{1/2}$ . The ensemble average in reference 10 is calculated using 60 surface realizations for each set of surface parameters  $\{h_{rms}, l_c\}$ . Monte Carlo simulations are carried out at 500 MHz for  $h_{rms} = 0.1\lambda$  to  $1\lambda$ ,  $l_c = 0.1\lambda$  to  $1\lambda$  in steps of  $0.1\lambda$ . As most realistic terrain surfaces have an *rms* height that is less than the correlation length, to reduce the number of simulation runs, only surface sets with  $h_{rms} \leq l_c$  are considered. Comparisons of the FDTD- and SIE-calculated backscattering coefficient for  $\theta_{inc} = 5^\circ, 10^\circ, 15^\circ$ , and  $45^\circ$  are shown in figures 3 and 4, for vertical and horizontal polarization, respectively. The error in the FDTD results is defined as

$\Delta = \sigma_{dB, FDTD}^o - \sigma_{dB, SIE}^o$ . Note that over the range of surface parameters of interest, very good agreement is observed between the two solvers for both polarizations, except for the region of small *rms* height and large correlation length (on the lower right corner of the figures—the “inaccurate” region) where the FDTD solution—at first glance—seems to deviate from the SIE solution. Outside this region, for vertical polarization, the average errors ( $|\overline{\Delta}|$ ) are 1.4 dB, 1.2 dB, 1.2 dB, and 0.8 dB for  $\theta_{inc} = 5^\circ, 10^\circ, 15^\circ$ , and  $45^\circ$ , respectively. Similarly, for horizontal polarization, the average errors are 1.4 dB, 1.3 dB, 1.1 dB, and 1.0 dB. Although the backscattering coefficient is the primary quantity of relevance in this study, for a more detailed comparison of the two solvers, the bistatic scattering patterns of the rough surface are analyzed in figures 5 and 6. Surface parameter sets in a region where FDTD is well behaved and in one where it deviates from the SIE solution are selected for comparison. It is seen that even for cases where erroneous results are observed in the backscattering directions, the FDTD routine still retains an accurate solution in the forward scattering directions—this stems from the fact that the

*relative* error is larger in the directions of weak scattering response, but the *absolute* error is likely the same throughout the range of observation angles.

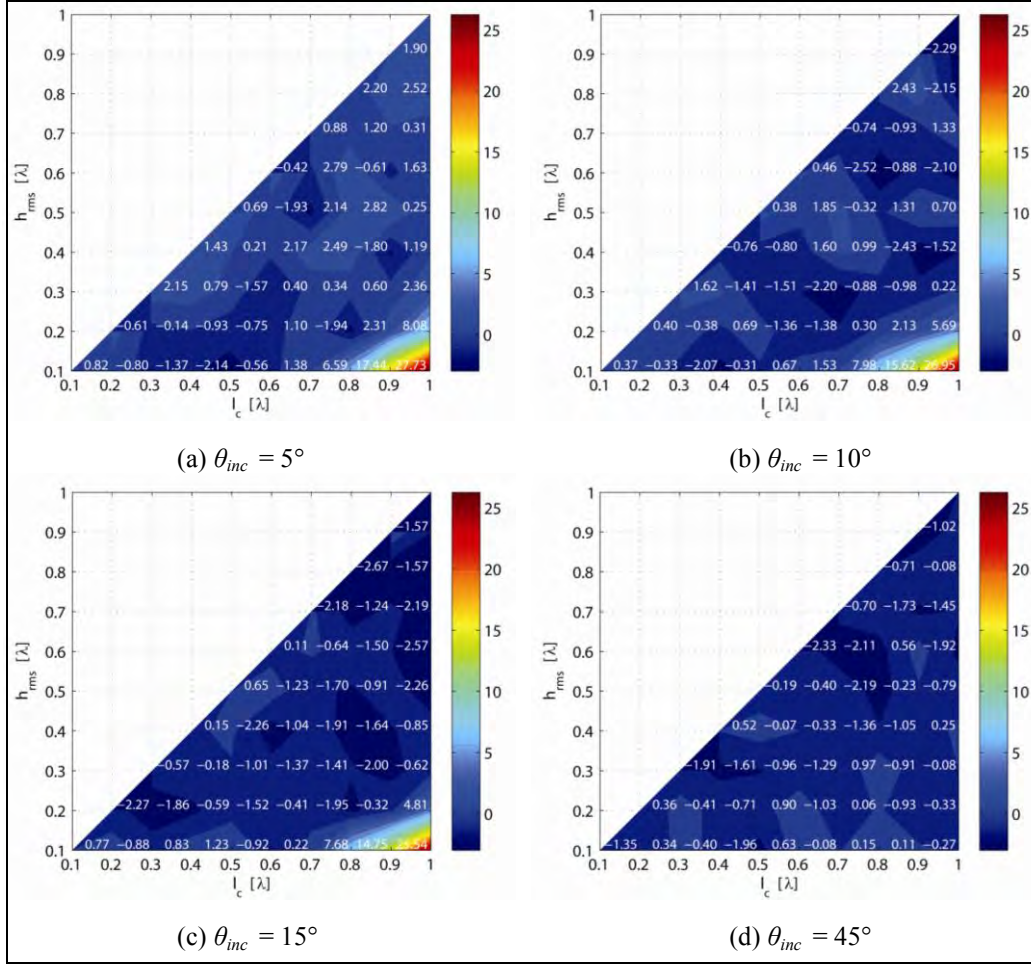


Figure 3. Errors ( $\Delta$  in dB) in the FDTD-calculated vertical-vertical (vv)-polarized backscattering coefficient ( $\sigma_{vv}^o$ )—as validated with the SIE solution—at various incidence angles for ground profiles characterized by Gaussian statistics  $\{h_{rms}, l_c\}$ ;  $\epsilon_r = 5.56$ ,  $\sigma_d = 10$  mS/m. Annotations at data points are shown, e.g., at  $\theta_{inc} = 5^\circ$ ,  $h_{rms} = 0.3\lambda$ ,  $l_c = 0.7\lambda$ ,  $\Delta = 0.40$  dB.

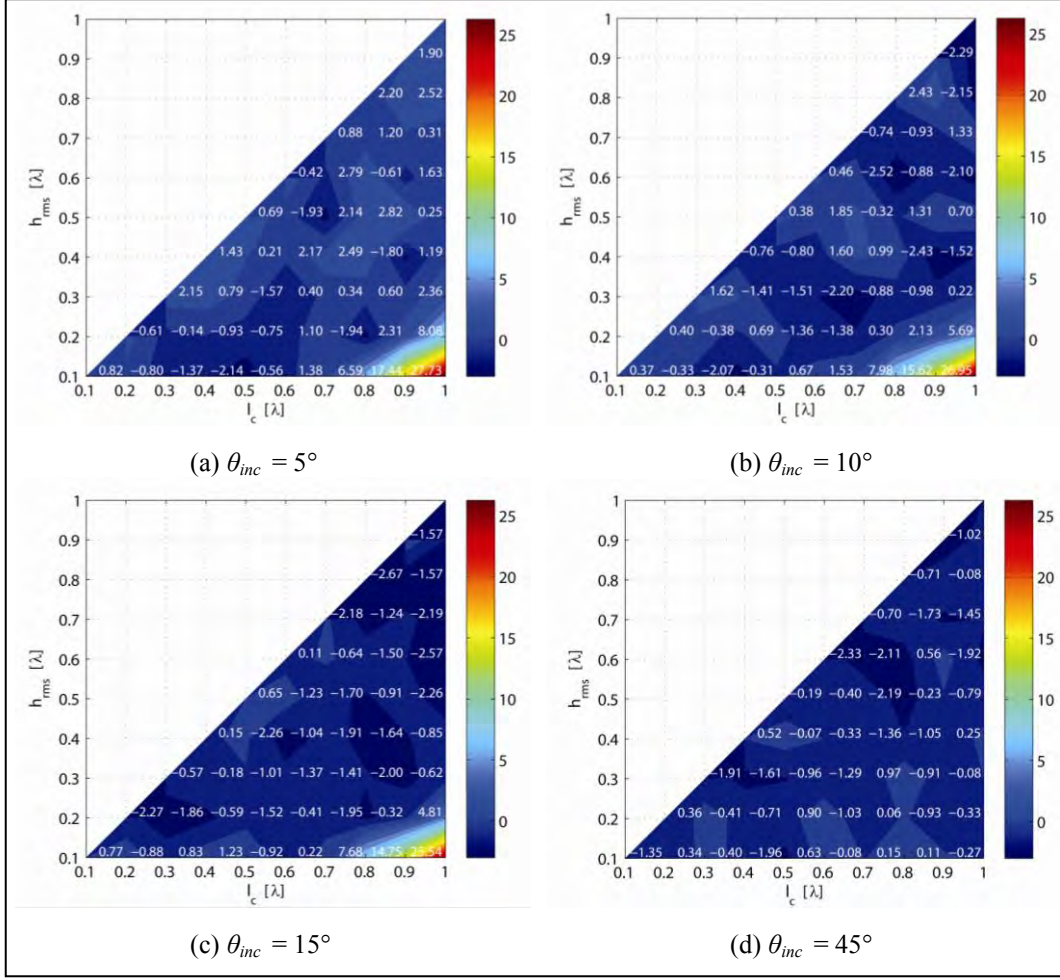


Figure 4. Errors ( $\Delta$  in dB) in the FDTD-calculated horizontal-horizontal ( $hh$ )-polarized backscattering coefficient ( $\sigma_{hh}^o$ )—as validated with the SIE solution—at various incidence angles for ground profiles characterized by Gaussian statistics  $\{h_{rms}, l_c\}$ ;  $\epsilon_r = 5.56$ ,  $\sigma_d = 10$  mS/m.

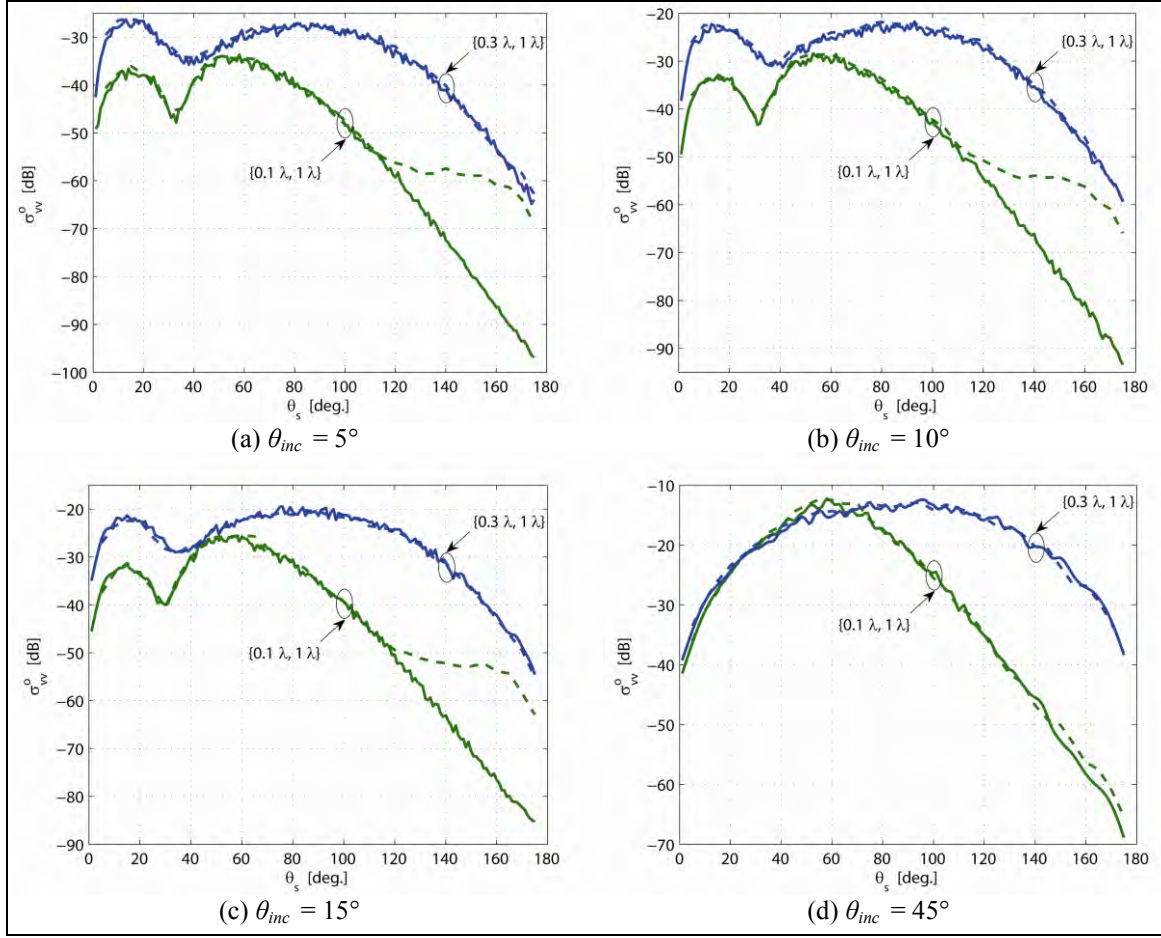


Figure 5. Comparison of vv-polarized bistatic scattering patterns as derived by SIE (solid lines) and FDTD (dash lines) at various incident angles for two sets of surface parameters:  $\{0.1\lambda, 1\lambda\}$  and  $\{0.3\lambda, 1\lambda\}$ ;  $\epsilon_r = 5.56$ ,  $\sigma_d = 10$  mS/m.



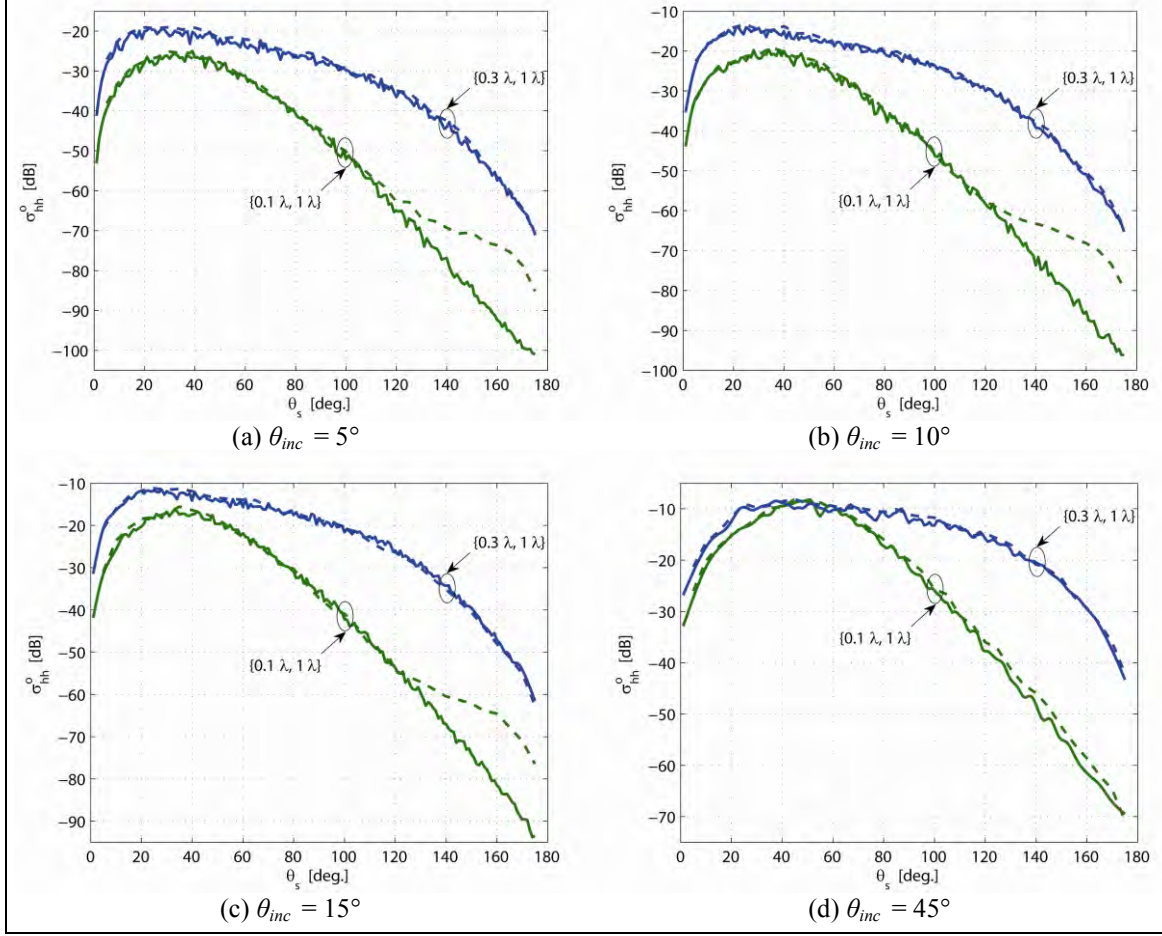


Figure 6. Comparison of  $hh$ -polarized bistatic scattering patterns as derived by SIE (solid lines) and FDTD (dash lines) at various incident angles for two sets of surface parameters:  $\{0.1\lambda, 1\lambda\}$  and  $\{0.3\lambda, 1\lambda\}$ ;  $\epsilon_r = 5.56$ ,  $\sigma_d = 10$  mS/m.

For all the simulations carried out in figures 3–6, the cell size is uniformly chosen to be  $0.01\lambda$ —though it is seen that a much coarser cell size can be used for surfaces with parameters located away from the “inaccurate” region. Figure 7 demonstrates that the aforementioned inaccuracies in the backscattering direction of the FDTD solution—for surfaces with small *rms* slope and large correlation length—can be reduced by further refining the FDTD grid. A smaller cell size, of course, means increased computational burden. It should be mentioned that increasing the length of the simulation domain (e.g., from  $10l_c$  to  $20l_c$ ) does not significantly improve the solution accuracy. Interestingly, the extremely weak backscattering responses generated by surfaces with small *rms* slopes also pose a challenge for the SIE solver, as the length of the simulation domain must be made large enough to guarantee the suppression of the edge diffraction effects. For instance, as seen in this study, for a surface with parameters  $\{0.3\lambda, 1\lambda\}$ , a surface length of  $4g$  is adequate; whereas, for a surface with parameters  $\{0.1\lambda, 1\lambda\}$ , a length of  $6g$  is needed.

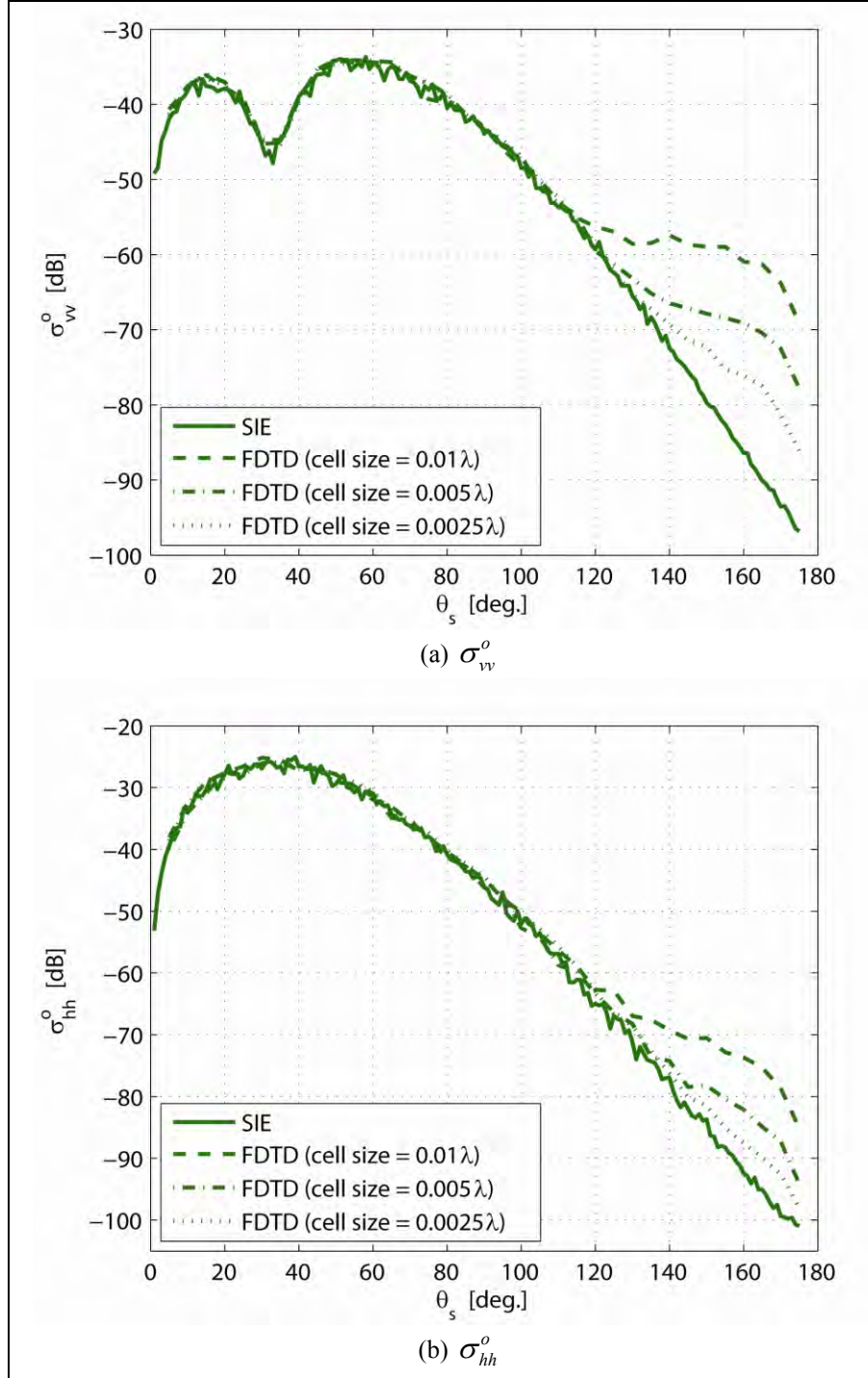


Figure 7. Convergence of FDTD solution as function of cell size for surface with parameters  $\{0.1\lambda, 1\lambda\}$ ;  $\epsilon_r = 5.56$ ,  $\sigma_d = 10$  mS/m;  $\theta_{inc} = 5^\circ$ .

---

### 3. Extension of FDTD Simulation of Rough Surface Scattering to 3-D

---

Though the solution to the 2-D scattering problem (for the 1-D surface) can convey important physical insights, only the full-wave vectorized solution to the 3-D scattering problem (for the 2-D surface) can provide a complete understanding of the scattering and propagation mechanisms, including cross-polarization interactions. Integral equation-based 3-D fast solvers devoted to analyzing rough surface effects have been proposed (44–47). For instance, the SDFMM (47) achieves  $O(N)$  complexity for both CPU time and memory requirements, as opposed to an unaccelerated scheme, which has  $O(N^2)$  complexity. As reported in literature, these fast algorithms have been applied for simulating only relatively small surfaces with non-grazing angle excitations. However, it should be mentioned that surfaces with dimensions up to  $256\lambda \times 32\lambda$  have been simulated by Torrungrueng and Johnson (48) in analyzing low-grazing angle effects. High-order routines and phase-extraction (23) can be used to explicitly reduce the number of unknowns in the integral equation method; however, no works have been done yet that take advantage of these techniques for the 3-D grazing scattering problem.

As complements to SIE routines, FDTD algorithms for studying scattering from 2-D rough surfaces have also been developed. In reference 49, the total field/scattered field (TF/SF) approach is used for zoning a computational lattice, which is, in turn, truncated by averaging boundary conditions instead of a PML. In the scattered field calculation stage, a windowing function is applied to the near-to-far-field transformation surface to reduce the boundary reflection effects. In reference 50, exploiting periodic boundary conditions, the 2-D surface is modeled as a periodic structure with one period of the surface extracted for FDTD computations. As the update equations in FDTD are inherently parallel in nature, Message-Passing Interface (MPI)-based routines also have been implemented to facilitate the simulation of large domains. The TF/SF algorithm in reference 51—developed specifically for studying rough surface scattering—adopts the uniaxial PML for terminating the computational domain and—similar to what is done in SIE routines—employs a Gaussian tapered incident wave to suppress truncation effects. Unfortunately, the focus of the aforementioned routines has been on non-grazing angle illuminations and the effectiveness of the various truncation boundary conditions and incident wave treatments for modeling the low-grazing angle scattering problem has not been studied.

In this work, the modeling of rough surface scattering is extended to the 3-D configuration by employing the AFDTD code. AFDTD (52) is a software package developed at ARL for radar signature calculation and is based on a 3-D implementation of the FDTD algorithm. The code is fully parallelized and runs on large distributed computer systems using the MPI framework. The computational domain is decomposed into rectangular subdomains and the FDTD equations are solved separately for each subdomain within one MPI process. Only the electric and magnetic field samples in the boundary layer between two adjacent subdomains need to be exchanged

between the respective processes (53). As a consequence, the AFDTD code is highly scalable, even when the number of MPI processes is in the hundreds. The rough surface scattering implementation for the 3-D AFDTD code follows closely the bounded surface perturbation approach presented in section 2 for the 2-D version. Random rough surfaces with isotropic statistical properties are examined in this section. Therefore, on average, the scattered power in the plane of incidence is independent of the azimuth incidence angle.

The expected range of validity (in terms of surface parameters and cell size) of the FDTD method has been examined in section 2. Further validation is performed by comparing 3-D Monte Carlo scattering results to measured data reported in reference 9. Two types of ground surface are considered: for figure 8,  $h_{rms} = 4$  mm,  $l_c = 8.4$  cm,  $\epsilon_r = 15.57$ , and  $\sigma_d = 0.31$  S/m; and for figure 9,  $h_{rms} = 3$  cm,  $l_c = 8.8$  cm,  $\epsilon_r = 8.92$ , and  $\sigma_d = 0.19$  S/m. The figures show there is good agreement between the simulated and measured backscattered responses (at 1.5 GHz) for  $20^\circ \leq \theta_{inc} \leq 80^\circ$  for both co-polarization components. Note the measured response includes a coherent component (which accounts for the strong peak observed in figure 8 near normal incidence) whereas the FDTD response does not. Also, while the FDTD-simulated surfaces are purely Gaussian, the measured profiles are of a more complex spectrum and can be fitted only approximately by Gaussian statistics—this perhaps explains the discrepancy seen near  $\theta_{inc} = 20^\circ$  for  $\sigma_{hh}^o$  in figure 8. Unfortunately, no empirical data can be found in literature at grazing angles less than  $20^\circ$  over the interested frequency range. The ensemble averages of the results from 30 surface realizations are shown in these figures: each surface realization has dimensions  $10l_c \times 10l_c$ ; solution convergence is observed with a FDTD grid size of 1 mm; the simulation of one realization at each incidence angle takes approximately 3 h on four 2.8-GHz Intel Nehalem processors, with a total memory load of 6.6 GB.



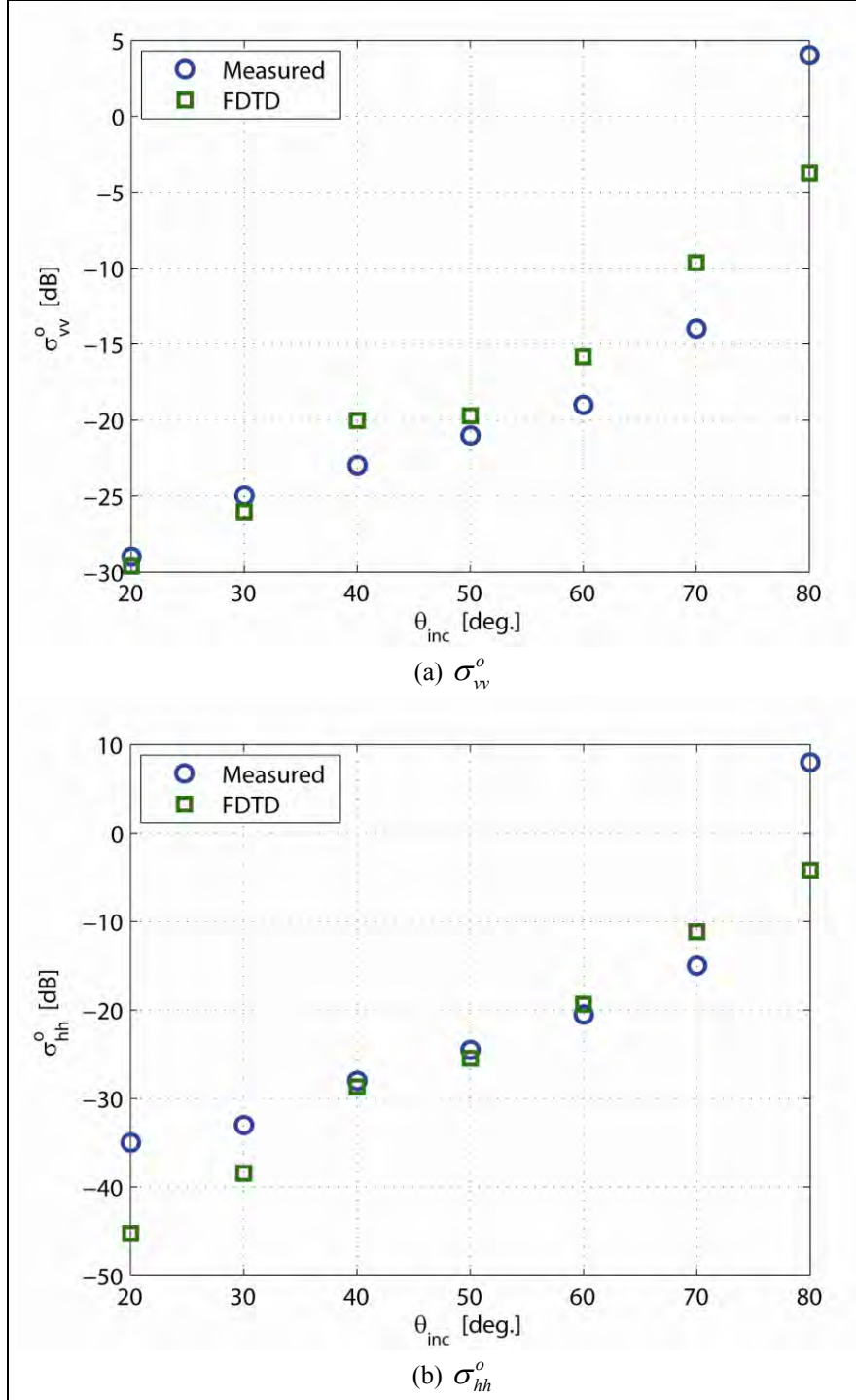


Figure 8. Comparison of FDTD-simulated 3-D backscattering results with measured data from reference 9:  $h_{rms} = 4$  mm,  $l_c = 8.4$  cm,  $\epsilon_r = 15.57$ , and  $\sigma_d = 0.31$  S/m. At angles close to normal ( $\theta_{inc} \rightarrow 90^\circ$ ), the strong measured response is due to the inclusion of a coherent surface reflection component; this component is not modeled in the simulations.

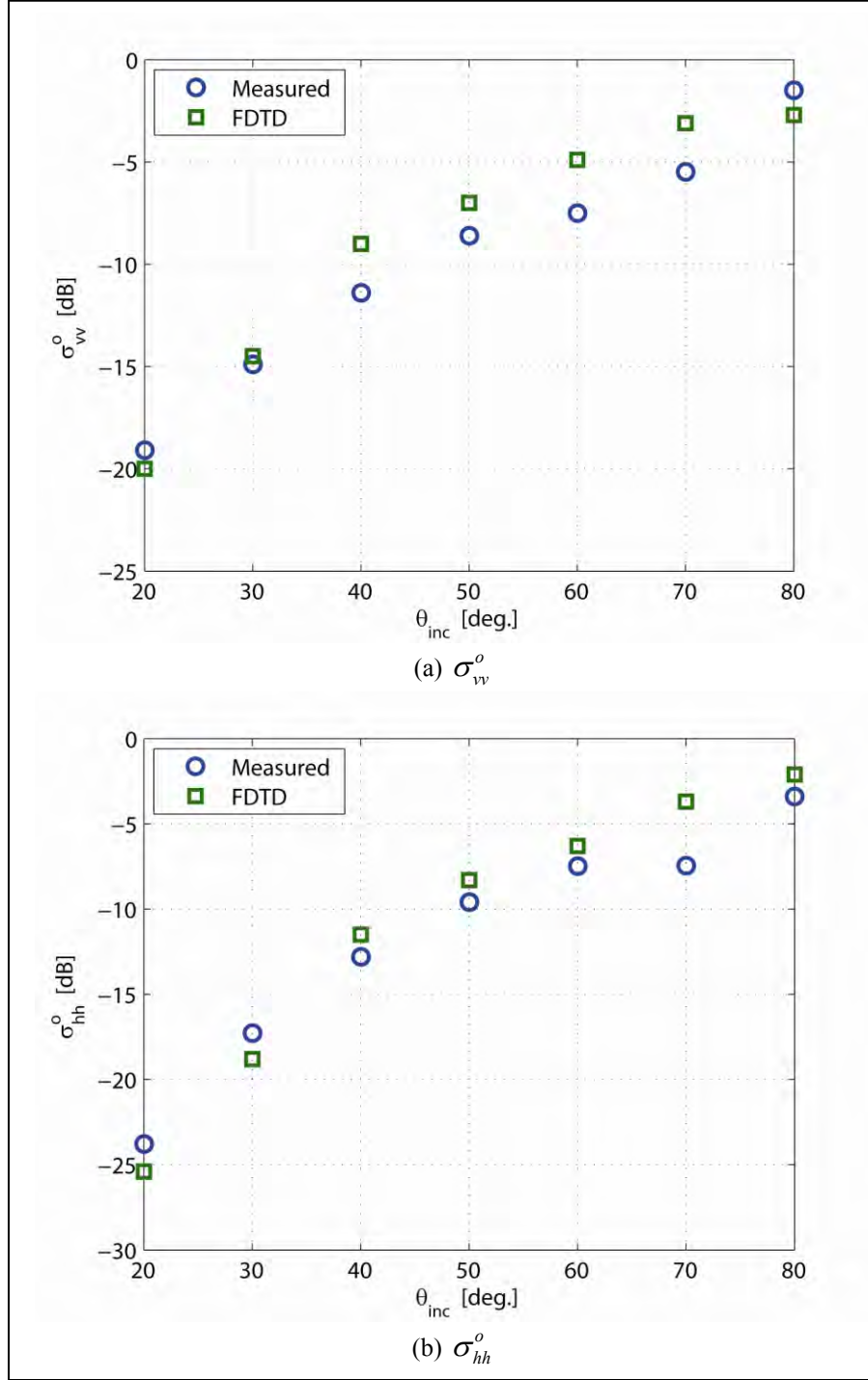


Figure 9. Comparison of FDTD-simulated 3-D backscattering results with measured data from reference 9:  $h_{rms} = 3$  cm,  $l_c = 8.8$  cm,  $\epsilon_r = 8.92$ , and  $\sigma_d = 0.19$  S/m.

The developed numerical tool is invaluable for studying the angular and spectral behaviors of ground clutter. Displayed in figure 10 is the backscattering coefficient—over the frequency band 500–2500 MHz, for  $5^\circ \leq \theta_{inc} \leq 15^\circ$ —of a typical surface with  $h_{rms} = 1$  cm,  $l_c = 7$  cm,  $\epsilon_r = 5.56$ , and  $\sigma_d = 10$  mS/m. It is observed that, in general, the backscattering power increases with the

grazing angle and  $\sigma_{vv}^o > \sigma_{hh}^o > \sigma_{hv}^o$  ( $\sigma_{vh}^o = \sigma_{hv}^o$  by reciprocity). Maximum surface scattering appears to be concentrated within 900–1500 MHz in this example. (The non-smooth nature of the intensity variations within the figures is a numerical artifact of the Monte Carlo simulations.) Qualitatively, the detectability of a specific target can be determined by simply comparing its scattering coefficient to that of the ground surface. A more complete consideration requires the intensity distribution of the ground response (in the image domain) to be studied. For the band of frequencies examined here, figure 10 shows that the amplitude of the surface response is increasing with frequency at the lower end of the band but decreasing with frequency at the higher end. This behavior is characteristic to Gaussian surfaces and consistent with results presented in a previous experimental study (54). Note that some real surface profiles may be of a more complex spectrum and can be only approximated by Gaussian statistics. In fact, the autocorrelation function of real natural terrain surfaces can be approximated to be Gaussian, exponential, or a combination of the two (9). The Gaussian surface is expected to be an adequate model at low frequencies where the fast surface variations inherent in an exponential spectrum are not sensed by the wave.

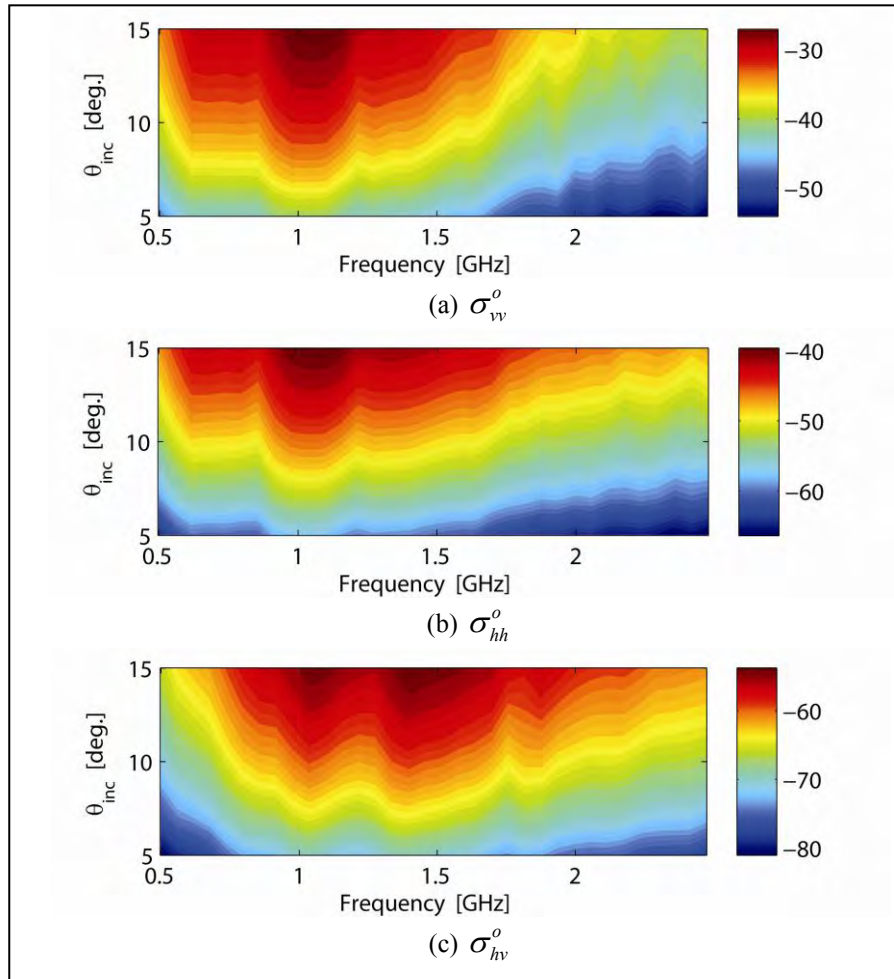


Figure 10. Angular and spectral distribution of backscattering from a rough surface with surface parameters  $h_{rms} = 1$  cm,  $l_c = 7$  cm,  $\epsilon_r = 5.56$ , and  $\sigma_d = 10$  mS/m.

---

## 4. Emulation of Forward-Looking Radar Imaging in Presence of Ground Clutter

---

Having studied the accuracy and region of validity of the proposed FDTD solver, large-scale full-wave modeling of multistatic target imaging in a rough ground environment is described in this section. An investigation of particular interest is the analysis of the statistics of the ground response in the images.

### 4.1 Emulation and Imaging Framework

First, the parallelized 3-D FDTD algorithm is applied to simulate composite scattering from targets in a rough ground environment. Then, a coherent field integration technique is employed to process the scattered signals to obtain an image of the illuminated scene. According to the time-reversal, or phase-conjugation, method (55, 56), since the received scattered field can be written as

$$E_s(\vec{r}_R, \vec{r}_T, \omega) = T(\omega) \alpha(\omega) G(\vec{r}_s, \vec{r}_T, \omega) G(\vec{r}_R, \vec{r}_s, \omega), \quad (11)$$

an approximate objective (image) function can be formed with the following expression:

$$O(\vec{r}) = \sum_{\omega} \sum_R \sum_T E_s^*(\vec{r}_R, \vec{r}_T, \omega) G(\vec{r}, \vec{r}_T, \omega) G(\vec{r}_R, \vec{r}, \omega); \quad (12)$$

where the asterisk notation denotes the phase conjugation operation;  $G(\vec{r}, \vec{r}', \omega)$  is the Green's function of the environment ( $\vec{r}$  is the position of the observation point and  $\vec{r}'$  is the position of the source point);  $\vec{r}_T$ ,  $\vec{r}_R$ , and  $\vec{r}_s$  are the locations of the transmitter, receiver, and scatterer, respectively; and  $T(\omega)$  and  $\alpha(\omega)$  are the spectra of the transmitted waveform and target response. The angular and range resolution of the image are determined by the sensor aperture and system bandwidth, respectively, of the coherent summation performed in equation 12. For sensing in the presence of a randomly varying ground interface, as the exact propagation Green's function is not known,  $G(\vec{r}, \vec{r}', \omega)$  is approximated by the half-space Green's function. As such, the target image is corrupted by ground clutter.

The effects of a rough ground surface on focusing are demonstrated with the simulation results displayed in figures 11–13, which show images of a 9 m × 19 m area populated with targets in the form of landmines (either anti-tank or anti-personnel, metallic or plastic, buried or on-surface) and 155-mm shells (metallic, buried). Specifically, the targets—the shapes, dimensions, orientations, and locations of which are indicated by the white outlines in image (a)—include the following:

1. Buried metallic anti-personnel landmine;

2. Buried plastic ( $\epsilon_r = 3.1$ ,  $\sigma_d = 2$  mS/m) anti-personnel landmine;
3. On-surface plastic ( $\epsilon_r = 3.1$ ,  $\sigma_d = 2$  mS/m) anti-personnel landmine;
4. Buried metallic 155-mm shell;
5. Buried metallic anti-tank landmine;
6. On-surface metallic anti-tank landmine;
7. Buried metallic 155-mm shell;
8. Buried metallic 155-mm shell;
9. On-surface metallic anti-personnel landmine;
10. Buried plastic ( $\epsilon_r = 3.1$ ,  $\sigma_d = 2$  mS/m) anti-tank landmine;
11. On-surface plastic ( $\epsilon_r = 3.1$ ,  $\sigma_d = 2$  mS/m) anti-tank landmine.

Buried targets are positioned at 3 cm below the surface.

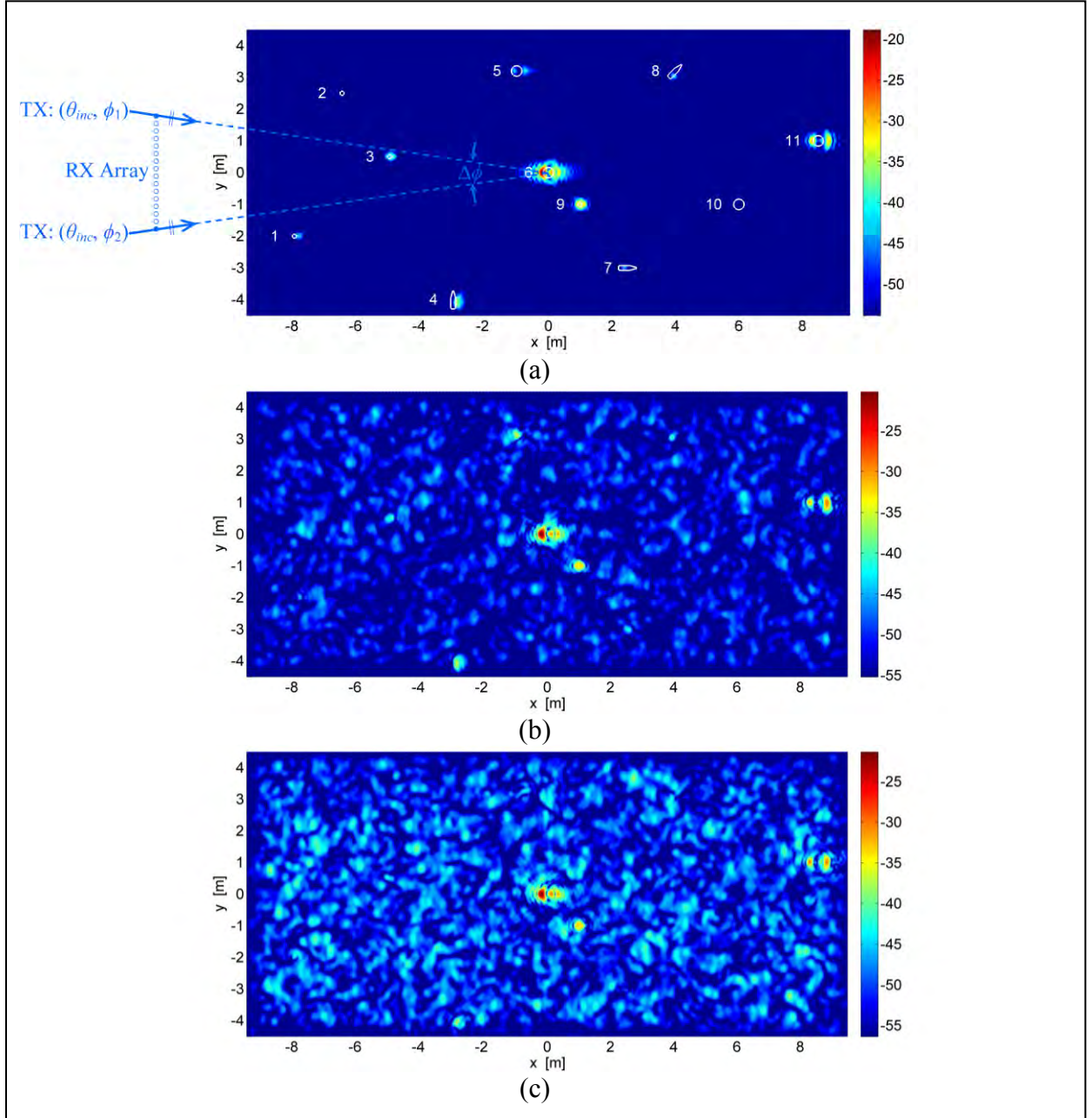


Figure 11. Simulated vv-polarized images for 9 m  $\times$  19 m scene: (a) Ground with flat surface; (b) ground with randomly rough surface,  $h_{rm} = 1.2$  cm,  $l_c = 14.93$  cm; and (c) ground with randomly rough surface,  $h_{rms} = 1.6$  cm,  $l_c = 14.93$  cm. Ground electrical properties:  $\epsilon_r = 8$ ,  $\sigma_d = 10$  mS/m.



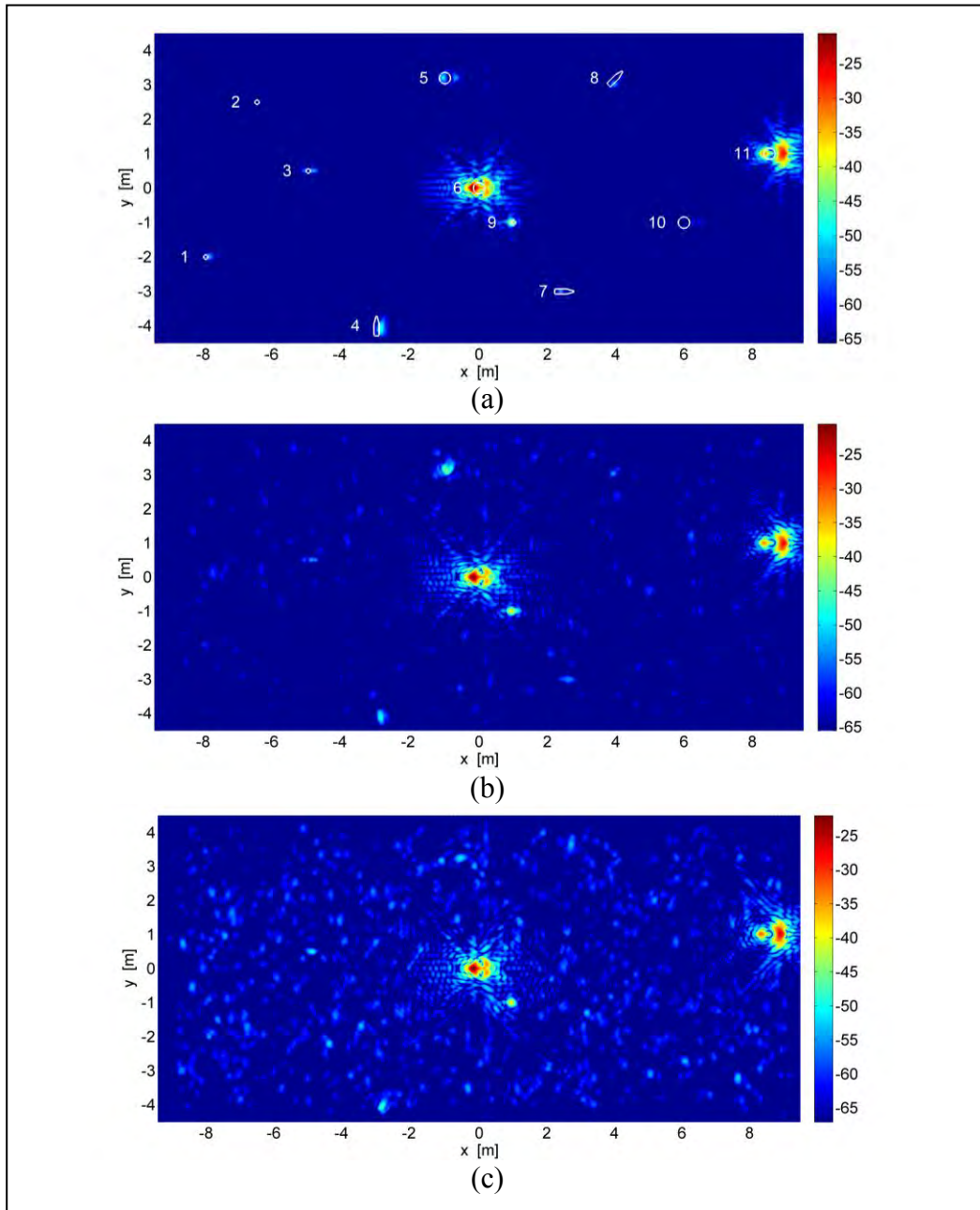


Figure 12. Simulated  $hh$ -polarized images for  $9\text{ m} \times 19\text{ m}$  scene: (a) Ground with flat surface; (b) ground with randomly rough surface,  $h_{rm} = 1.2\text{ cm}$ ,  $l_c = 14.93\text{ cm}$ ; and (c) ground with randomly rough surface,  $h_{rms} = 1.6\text{ cm}$ ,  $l_c = 14.93\text{ cm}$ . Ground electrical properties:  $\epsilon_r = 8$ ,  $\sigma_d = 10\text{ mS/m}$ .

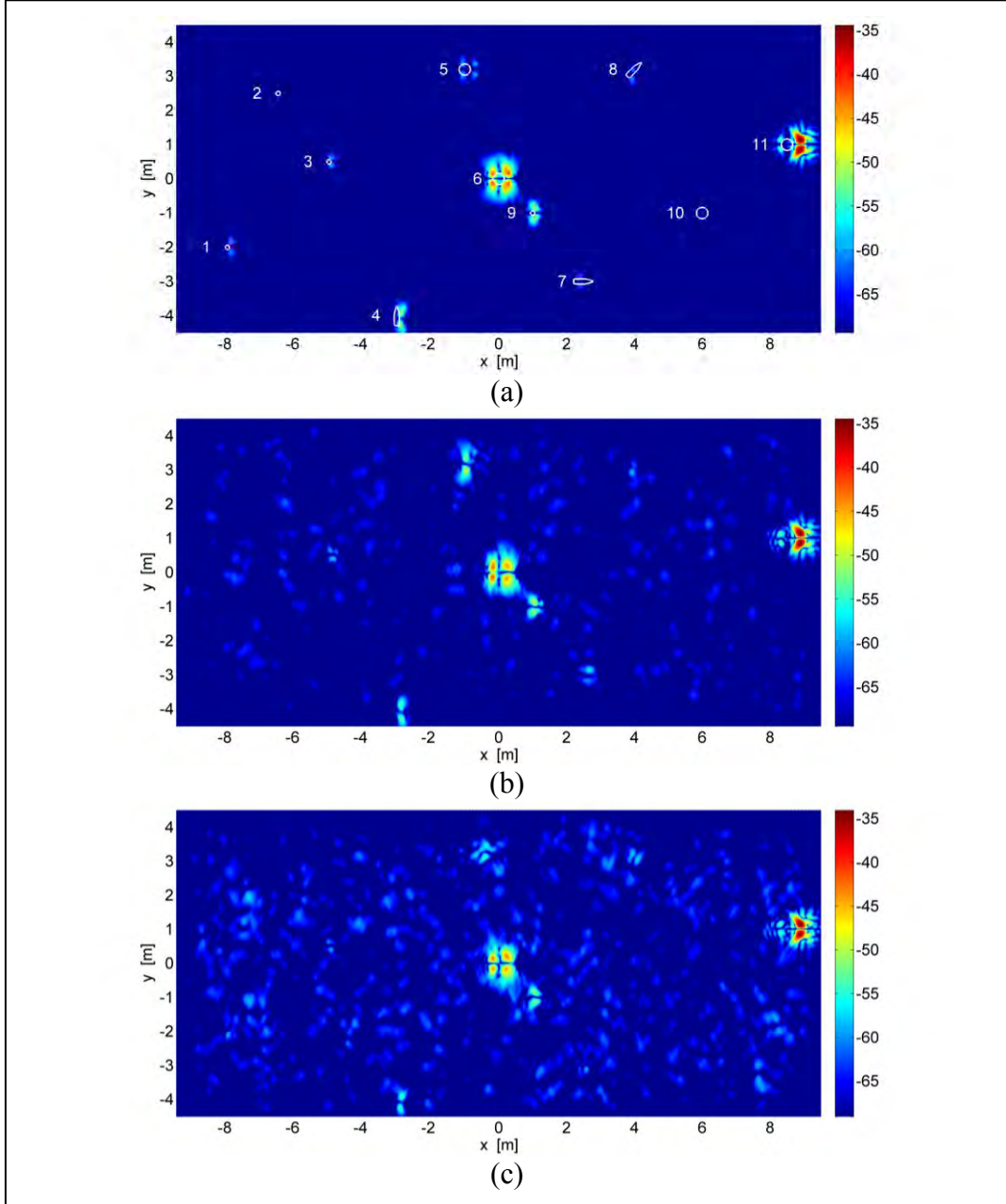


Figure 13. Simulated  $h\nu$ -polarized images for  $9\text{ m} \times 19\text{ m}$  scene: (a) Ground with flat surface; (b) ground with randomly rough surface,  $h_{rm} = 1.2\text{ cm}$ ,  $l_c = 14.93\text{ cm}$ ; and (c) ground with randomly rough surface,  $h_{rms} = 1.6\text{ cm}$ ,  $l_c = 14.93\text{ cm}$ . Ground electrical properties:  $\epsilon_r = 8$ ,  $\sigma_d = 10\text{ mS/m}$ .

At this point, some important differences between the configuration of the SIRE radar and the setup of the simulation scenario should be mentioned. The SIRE radar transceiver consists of an array of equally spaced receivers placed across a linear aperture and two transmitters situated at the ends of the aperture. The entire assembly is elevated at 2-m height (atop a vehicle) and covers downrange between 8 and 21 m while the platform is on the move. (To be specific, the radar height can be varied from 2 to 3 m; in field experiments, the downrange coverage is from



8 to 33 m, although only the captured scattered fields corresponding to a distance of 8 to 21 m are used for image formation.) Since AFDTD only implements incidence and scattering in the far-field, plane-wave incidence from two azimuth directions and five elevation angles that span the same solid angle as the SIRE transmitters is considered. For each elevation angle, the bistatic scattered fields are computed at equally spaced azimuth angles (in  $1^\circ$  increments) that provide similar azimuth coverage as the SIRE receivers. At the limits of the SIRE radar range coverage, the elevation angles and angular apertures correspond to  $\theta_{inc} = 5^\circ$ ,  $\Delta\phi = 32^\circ$  and  $\theta_{inc} = 15^\circ$ ,  $\Delta\phi = 77^\circ$ , respectively. The FDTD simulations were performed at the ARL Distributed Supercomputing Resource Center (DSRC) in Aberdeen, MD, on a SGI Altix ICE 8200 system. The discretization of the entire  $9\text{ m} \times 19\text{ m}$  scene involved 1.9 billion cells, and each simulation run at one incidence angle required 256 processors and approximately 2000 CPU hours.

## 4.2 Results and Discussions

The co- and cross-polarization images generated from the full-wave simulation data are displayed in figures 11–13, where three ground roughness scales are examined: (a) flat ground; (b)  $h_{rms} = 1.2\text{ cm}$ ,  $l_c = 14.93\text{ cm}$ ; and (c)  $h_{rms} = 1.6\text{ cm}$ ,  $l_c = 14.93\text{ cm}$ . The response from the larger targets (anti-tank landmines) in the backscattering directions is primarily due to edge diffractions from the front and back rims of the top of the cylindrical structure. The scattering centers corresponding to these two edges are resolved in the images—for both on-surface and buried cases. For the smaller targets (anti-personnel landmines), the two scattering edges tend to merge into one, since the imaging configuration as chosen here is unable to provide sufficient resolution to separate the two phase centers. In the presence of a rough ground interface, these diffraction effects are less apparent in the images for the buried targets due to interference from surface scattering. Buried targets are generally more difficult to discern from the background as compared to on-surface targets. For instance, the co-polarized intensity of the buried metallic anti-tank landmine is about 15 to 20 dB below that of the on-surface configuration—for a ground with either a flat or rough surface. The difference for the cross-polarized return is less, at 8 to 10 dB. A buried plastic target (either large or small landmine) is especially hard to detect owing to the limited dielectric contrast between the target and the soil background. The orientation of a target can also have a significant impact on its radar return: maximum response from the 155-mm shell is observed when it is oriented parallel to the imaging aperture. A much weaker response is noted when it is oriented perpendicular or obliquely (at  $45^\circ$ ) to the aperture. These observations are consistent with the analysis previously reported by reference 57.

Comparing all target responses across the three polarizations, on average,  $vv$  provides the strongest response, and it exceeds  $hh$  by about 10 dB (except for the large on-surface landmines). The  $hh$  polarization, in turn, exceeds the cross-polarization response by about 7 dB. For the large on-surface landmines (either metallic or plastic), the two co-polarization components are approximately equal in intensity due to grazing angle incidence. (At steeper incidence angles, the  $hh$  response is generally larger as a result of enhanced ground bounce contribution). However, when these targets are buried,  $vv$  again seems to give the stronger return. As a vertically

polarized signal experiences less transmission loss at the air-ground interface and suffers less propagation loss in general, the above observation supports the notion that  $vv$  is the more desirable configuration for detecting targets either on top of or buried under a flat ground. In the presence of ground surface roughness, detection performance must be evaluated with a consideration of the target-to-background clutter ratio. As such, since the surface response is strongest at  $vv$ , vertical polarization does not seem to provide an advantage—as seen in figures 11c, 12c, and 13c, where certain buried targets (i.e., targets 4 and 5) are found to stand out against the background more in  $hh$  and horizontal-vertical ( $hv$ ) than in  $vv$ .

It is interesting to also note the “butterfly-shaped” formation generated by each point target in the  $hv$ -polarized images: two pairs are observed for the anti-tank landmines and one pair for other smaller targets. An explanation for the appearance of this feature can be derived by realizing that—for a vertically polarized (or  $E_\theta$ -polarized) incident wave—although the induced currents on the targets are flowing mostly in both the vertical (parallel to  $z$ -axis) and downrange (parallel to  $x$ -axis) directions, only the downrange-oriented currents can generate any cross-polarized ( $E_\phi$ ) field component. As a result, since the  $E_\phi$  component of the scattered field from these downrange currents is anti-symmetric (that is, equal in amplitude, opposite in sign) about the direction of the incidence wave, integration of fields due to excitation from two incidence angles ( $\phi_1$  and  $\phi_2$ ) over the same angular span  $\Delta\phi$  leads to the formation of a null at the center of the target image pattern. For point-like, discrete targets, although symmetry in the target structure helps in establishing a stronger response for this “butterfly-shaped” pattern, it is not a necessary condition: the same pattern is observed for the 155-mm shell (targets 4, 7, and 8) as well. This distinctive feature mentioned could be exploited for target identification in detection algorithms, but one should note that a very rough ground surface could exhibit many peaks acting as strong point scatterers and, in turn, generating the same type of feature.

The images of figures 11–13 essentially map the spatial variation of the average radar cross section (RCS) of the scene, where the averaging operation, equation 12, is being carried over a range of frequencies and observation angles in elevation and azimuth. An overlay of the images on the physical surface profile suggests that the brightest surface returns are from the surface peaks—or, more specifically, from the faces of the surface peaks that are oriented toward the radar. This is different from radar observations at larger incidence angles, for which both the peaks and troughs of the surface could produce strong returns. As the roughness scale increases, at grazing angles, it is also expected that the shadowing effect would play a significant role in determining the total surface return. Curiously, in reviewing the rough ground image data, the  $vv$  response is seen to be much greater than both the  $hh$  and the cross-polarized responses as expected, but the  $hh$  response itself is only slightly greater than the cross-polarized response. For example, according to figures 11b, 12b, and 13b, the mean ground clutter,  $\bar{\sigma}_{dB}^c$ , is calculated to be  $-55.12$  dB for  $vv$ ,  $-71.50$  dB for  $hh$ , and  $-74.60$  dB for  $hv$ , while a study of the backscattering coefficients (within the same frequency band) for the same ground properties reveals that the  $hh$  response is 10 to 19 dB higher than the  $hv$  response. (The large difference between the

amplitudes of the  $vv$  and  $hh$  responses is a result of observation at near-grazing angles and the use of Gaussian statistics for the ground surface. In view of the lack of experimental data at these grazing angles, it is unclear whether this large difference is also evident in actual measurement results for real surfaces of a more complex spectrum.) The discrepancy between the imaging and backscattering results can be resolved by analyzing the bistatic scattering pattern of the rough surface and noting that the cross-polarized response can become greater than the  $hh$  response away from the incidence direction  $\phi_{inc}$ . In fact, at low elevation angles and over the range of azimuth angles ( $\Delta\phi < 90^\circ$ ) of interest in this study, the  $hv$  scattering pattern has a minimum at  $\phi_{inc}$  but quickly increases in intensity away from that direction. On the other hand, the  $hh$  response tends to remain constant or even decrease over the same range of observation angles. Consequently, the average response taken over  $\Delta\phi$  may lead to a higher cross-polarized image response relative to  $hh$  than as indicated by backscattering analysis alone. For grazing-angle observations, it is noted that these behaviors of the  $hh$  and cross-polarized responses (in azimuth) are equally applicable to an on-surface or shallow-buried point-like, discrete target.

The vertical-horizontal ( $vh$ )-polarized images for the scene examined in figures 11–13 are not included here but are seen to be very similar to the  $hv$  case. It should be mentioned that given the bistatic sensing geometry used in this work, the reciprocity principle cannot be exploited for direct inference of the  $vh$  response from the  $hv$  one, or vice versa.

To quantify target detection performance, the distribution of the ground response needs to be estimated. Once the image clutter distribution is known and an acceptable false-alarm rate chosen, a threshold value for the detectability of a target of a given RCS can be determined. For a statistically homogeneous terrain scene, in the absence of multipath and shadowing effects, the scattered field response (i.e., equivalently, the amplitude of the scattering matrix elements,  $|S_{pq}|$ , or radar voltage response) is commonly found to conform to Rayleigh statistics (58). In other words, the real and imaginary parts of  $S_{pq}$  are observed to be uncorrelated zero-mean Gaussian random variables with equal variances. Other distributions also have been proposed to account for terrain scenes exhibiting more complex and non-Gaussian scattering phenomena. Examples include the lognormal, Weibull, and  $K$ -distributions. A study of the surface clutter in the simulated images derived in this work indicates that while a Rayleigh fading model is adequate for surfaces with small *rms* slopes, a  $K$ -distribution is seen to be more appropriate at larger *rms* slopes. As the  $K$ -distribution—which is a mixture of a Rayleigh and Gamma distribution—can be reduced to Rayleigh as a special case (59), the  $K$ -distribution is used henceforth as the basis to model the rough ground response.

In the image domain, the probability density of the pixel intensities (i.e., the scattered power response  $\sigma_{dB}^c$ , expressed in decibel) is found to be a very good match to the function

$$p(\sigma_{dB}^c | \nu, \xi) = \frac{\ln 10}{10} \cdot \frac{1}{2^{\nu+1} \Gamma(\nu+1)} \left( \frac{\sqrt{s}}{\xi} \right)^{\nu+2} K_\nu \left( \frac{\sqrt{s}}{\xi} \right), \quad (13)$$

where  $-1 < \nu < \infty$ ;  $\xi > 0$ ;  $s = 10^{\sigma_{dB}^c/10}/4\pi$ ;  $\Gamma(\cdot)$  is the Gamma function; and  $K_\nu(\cdot)$  is the modified Bessel function of the second kind of order  $\nu$ . The parameter  $\nu$  controls the shape of the density function, with  $\xi$  as a scaling factor. It is important to note that  $\sigma_{dB}^c$  itself is not  $K$ -distributed, though expression 13 is derived here by assuming a  $K$ -distribution for the scattered field amplitude. Also, note for large argument  $\nu$ , it can be shown that

$$p(\sigma_{dB}^c | \nu \rightarrow \text{large}, \xi) \approx \frac{\ln 10}{10} \cdot \frac{s}{\bar{\sigma}^c} e^{-\frac{s}{\bar{\sigma}^c}}, \quad (14)$$

where

$$\bar{\sigma}^c \approx \frac{16}{\pi} \left[ \frac{\xi \Gamma(1.5) \Gamma(\nu + 1.5)}{\Gamma(\nu + 1)} \right]^2. \quad (15)$$

Expression 14 is the distribution corresponding to Rayleigh-based fading statistics with mean power  $\bar{\sigma}^c$  (in linear scale). As the  $K$ -distribution model was originally developed for analyzing sea clutter, its applicability to ground surface returns is not fully understood. Nevertheless, it has been successfully used for describing a wide range of land clutter (60, 61).

The distributions of the  $\nu\nu$ -polarized ground response for the previously imaged  $9 \text{ m} \times 19 \text{ m}$  scene are displayed in figure 14. Four ground roughness levels are considered:  $h_{rms} = 1.2 \text{ cm}$ ,  $1.6 \text{ cm}$ ,  $2.0 \text{ cm}$ , and  $2.4 \text{ cm}$ ;  $l_c$  is kept constant at  $14.93 \text{ cm}$  for the four cases. (The images for  $h_{rms} = 1.2 \text{ cm}$  and  $1.6 \text{ cm}$  are shown in figures 11a and 11b, respectively.) The histograms are formed directly using the image data for the scene simulated with the targets removed. The distribution  $p(\sigma_{dB}^c | \nu, \xi)$  is seen to provide an excellent fit to the full-wave simulated response: (a)  $\nu = 100$ ,  $\xi = 3.31 \times 10^{-5}$ ; (b)  $\nu = 12$ ,  $\xi = 1.25 \times 10^{-4}$ ; (c)  $\nu = 10$ ,  $\xi = 1.65 \times 10^{-4}$ ; and (d)  $\nu = 8$ ,  $\xi = 2.06 \times 10^{-4}$ . A smaller value for  $\nu$  signifies a longer “tail” in the amplitude distribution of the ground response—implying there is a greater probability for the occurrence of strong scattering points within the scene. A manifestation of this effect is readily seen in the images. For example, even though the mean value of the ground response for  $h_{rms} = 2.4 \text{ cm}$  (case (d)) is only slightly greater than that for  $h_{rms} = 2.0 \text{ cm}$  (case (c)), the image for case (d) appears more cluttered due to the presence of a larger population of bright clusters of scattering centers.

Figure 14 shows that for a relatively smooth ground surface (case (a)), Rayleigh scattering is a reasonable descriptor, but as roughness increases, the scattering statistics tend to deviate from Rayleigh. One of the generally held tenets of the Rayleigh model is that the number of scatterers within a resolution cell must be large. As such, the central limit theorem can be invoked in characterizing the received signal as a vector sum of many samples of random phasors. Given that requirement, as well as the high resolution of the images considered here (i.e., few scatterers in each resolution cell), the observation that the Rayleigh model can be applied for small roughness scales is rather unexpected. However, it is conjectured here that because of the wide

observation angle (in  $\phi$ ) and the multi-aperture (in  $\theta$ ) configuration used for the imaging geometry, the received signal for a gently varying surface can still be thought of as the sum of many random independent samples of the scattered field.

The deviation from the Rayleigh scattering process observed for cases (b)–(d) can be attributed to the appearance of an increased number of strong point-like scatterers in a rougher surface. These point-like scatterers, or scattering centers, tend to radiate in a more directional and less-random manner. Thus, the requirement for independent random sampling may be violated. In addition, note that surface self-shadowing and higher order (or multiple) scattering begin to play a more significant role in determining the total signal return at larger surface roughnesses, and these effects are further accentuated at low-grazing angles. That confirms the well-known fact that shadowing and multipath effects can lead to a departure from Rayleigh scattering statistics (62). Similar analysis as above demonstrates that expression 13 is also a reasonable model for the ground response in the  $hh$ -,  $hv$ -, and  $vh$ -polarized images. Of the four polarization combinations, the distributions for  $hh$  are seen to deviate from Rayleigh statistics the most, while the distributions for the cross-polarized components are seen to lie somewhere between those of the  $vv$  and  $hh$  cases. This observation is consistent with previously reported results on the dependency of scattering distribution on polarization (63).

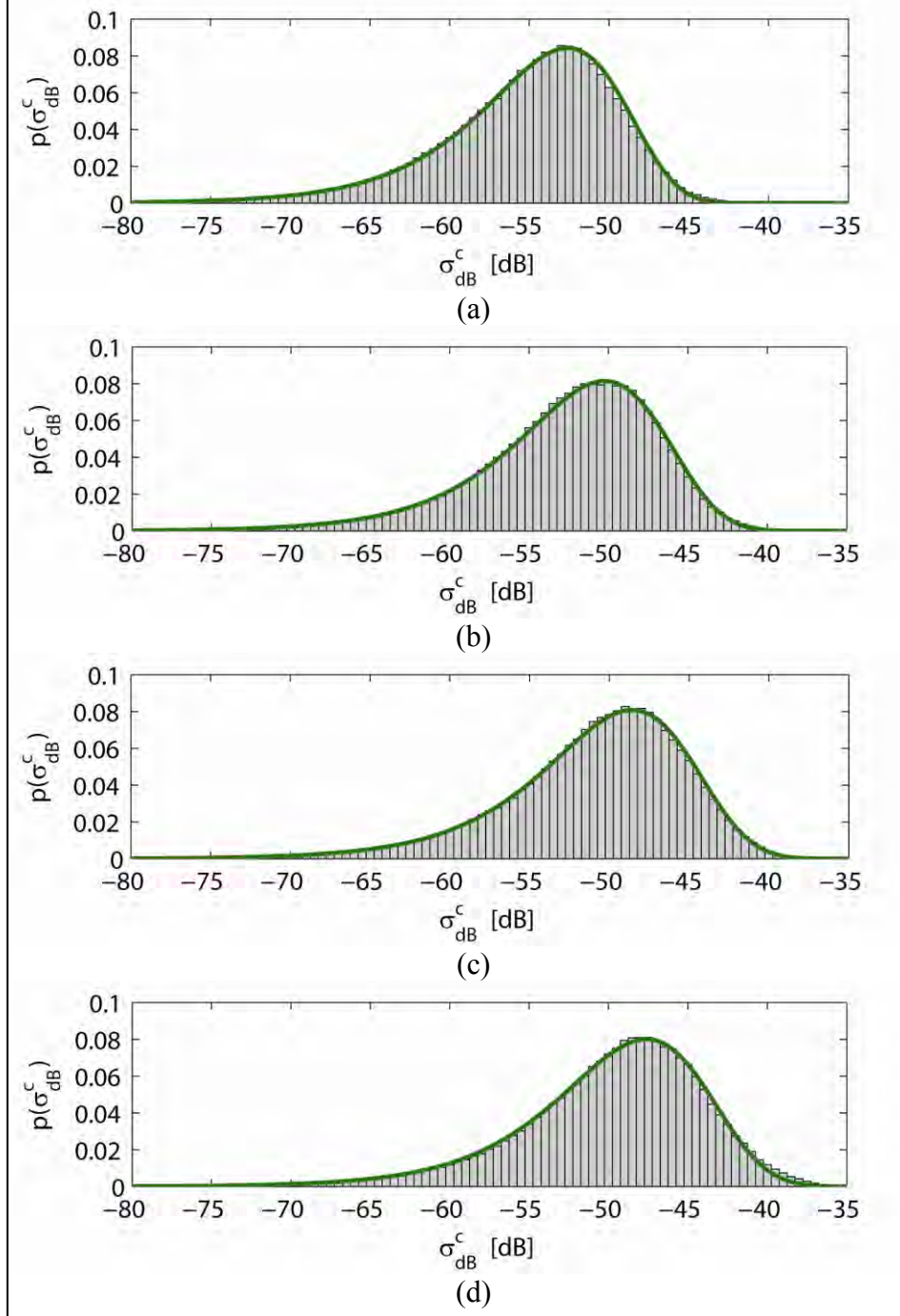


Figure 14. Probability density of  $vv$ -polarized ground response: histogram shows the distribution inferred from simulated images; solid line is distribution calculated using expression 13. Ground with randomly rough surface: (a)  $h_{rms} = 1.2$  cm,  $l_c = 14.93$  cm; (b)  $h_{rms} = 1.6$  cm,  $l_c = 14.93$  cm; (c)  $h_{rms} = 2.0$  cm,  $l_c = 14.93$  cm; and (d)  $h_{rms} = 2.4$  cm,  $l_c = 14.93$  cm. Ground electrical properties:  $\epsilon_r = 8$ ,  $\sigma_d = 10$  mS/m.

---

## 5. Conclusion

---

A FDTD-based solver is proposed for characterizing the electromagnetic scattering behavior of rough ground surfaces at low depression angles. The simulation approach employs a finite-extent surface perturbation model for the interface and a coherent error subtraction technique for reducing numerical dispersion artifacts. The regions of validity of the solver have been investigated for 1-D surfaces by comparing Monte Carlo scattering results to those from a high-order SIE approach for various surface parameters and incidence angles. Backscattering coefficients of 2-D random surfaces as computed with the MPI-based, parallelized FDTD code display good agreement with measurement data available in literature. The study indicates that the overall FDTD framework described herein is a promising approach for modeling the grazing scattering effects of a wide range of surfaces encountered in practical radar sensing. Inaccuracies have been noted, however, when the surfaces exhibited at once small *rms* slope *and* large correlation length—parameters yielding geometrical variations that are difficult to model correctly within the stair-stepped approximation of the FDTD grid. Although not shown here, if the results were extrapolated for the treatment of surfaces exhibiting large *rms* slope *and* small correlation length, the FDTD algorithm is expected to encounter difficulties for that case as well. The aforementioned limitations and errors can be mitigated by refining the computational lattice. Another possible improvement would be implementing a non-uniform lattice that uses finer cells around the ground interface region (64), or using stretched Yee cells, in which one dimension is larger than the others (38). With respect to the proper selection of the rough surface spectra (or autocorrelation function), this work focuses mostly on Gaussian surfaces. However, the numerical analysis methods are more general and can be applied to realistic surfaces of arbitrary spectra (including multi-scale models).

As compared to conventional SIE, the proposed FDTD algorithm is expected to be a more computationally viable option for analyzing grazing-angle scattering phenomena, since it necessitates a smaller simulation domain with horizontal dimensions that are independent of the incidence angle. Additionally, the FDTD technique can easily accommodate hybrid scattering scenarios, where targets of almost arbitrary shape and material composition can be included together with a rough air-ground interface, as well as soil inhomogeneities.

In demonstrating the usefulness of the developed solver as pertinent to forward-looking radar sensing, the effects of surface clutter on multistatic target imaging are illustrated with large-scale simulations of a realistic scene consisting of targets embedded in a rough ground environment. A study of the ground response in the image domain shows that the *K*-distribution provides a reasonable model for characterizing the statistics of the rough surface multistatic, wideband radar return.

Collectively, the formalisms, results, and observations featured in this study represent the first step taken in understanding and predicting the impact of ground surface clutter on the detection performance of a low-frequency imaging radar operating at close-to-grazing angles. Future work will include more realistic models of the SIRE radar geometry (which could better be described by a near-field configuration) and its antenna patterns, as well as the roughness characterizing the terrain.



---

## 6. References

---

1. Ressler, M.; Nguyen, L.; Koenig, F.; Wong, D.; Smith, G. The ARL Synchronous Impulse Reconstruction (SIRE) Forward-looking Radar. *Proc. SPIE* **May 2007**, 6561.
2. Kositsky, J.; Cosgrove, R.; Amazeen, C.; Milanfar, P. Results From a Forward-looking GPR Mine Detection System. *Proc. SPIE* **April 2002**, 4742.
3. Bradley, M.; Witten, T.; Duncan, M.; McCummins, B. Mine Detection with a Forward-looking Ground-penetrating Synthetic Aperture Radar. *Proc. SPIE* **April 2003**, 5089.
4. Wang, J.; Li, Y.; Zhou, Z.; Jin, T.; Yang, Y.; Wang, Y. Image Formation Techniques for Vehicle-Mounted Forward-Looking Ground-Penetrating SAR. *Proc. Intl. Conf. Info. Automat.*, Jun. 2008.
5. Billingsley, J. B. *Ground Clutter Measurements for Surface-sited Radar*; Technical Report 786, rev. 1, Lincoln Laboratory: Lexington, MA, Feb. 1993.
6. Billingsley, J. B. *Low Angle Radar and Clutter: Measurements and Empirical Models*; William Andre Publishing: Norwich, NY. 2002.
7. Morchin, W. *Radar Engineer's Sourcebook*; Artech House: Boston, MA. 1993.
8. Ulaby, F. T.; Dobson, M. *Handbook of Radar Scattering Statistics for Terrain*; Artech House: Boston, MA. 1989.
9. Oh, Y.; Sarabandi, K.; Ulaby, F. T. An Empirical Model and an Inversion Technique for Radar Scattering From Bare Soil Surfaces. *IEEE Trans. Geosci. Remote Sensing* **March 1992**, 30 (2), 370–381.
10. Rice, S. O. Reflection of Electromagnetic Wave by Slightly Rough Surfaces. *Commun. Pure Appl. Mathem.* **1951**, 4, 351–378.
11. Ishimaru, A. *Electromagnetic Wave Propagation, Radiation, and Scattering*; Prentice Hall: Englewood Cliffs, N.J., 1991.
12. Beckman, P.; Spizzichino A. *The Scattering of Electromagnetic Waves from Rough Surfaces*; Pergamon: New York, 1963.
13. Johnson, J. T. Third-Order Small-Perturbation Method for Scattering From Dielectric Rough Surfaces. *J. Opt. Soc. Am. A* **November 1999**, 16 (1), 2720–2736.
14. Dermir, M. A.; Johnson, J. T. Fourth and Higher Order Small Perturbation Solution for Scattering From Dielectric Rough Surfaces. *IEEE Antennas and Propagat. Soc. Symposium Digest* **2003**, 412–415.

15. Voronovich, A. *Wave Scattering From Rough Surfaces*; Heidelberg: Springer. 1994.
16. Gilbert, M. S.; Johnson, J. T. Implementation of the Higher Order Small Slope Approximation for Scattering From a Gaussian Rough Surface. *IEEE Geosci. Remote Sens. Symposium Digest* **2002**, 1260–1262.
17. Winebrenner, D.; Ishimaru, A. Investigation of a Surface Field Phase Perturbation Technique for Scattering From Rough Surfaces. *Radio Sci.* **March/April 1985**, 20 (2), 161–170.
18. Rodriguez, E.; Kim Y. A Unified Perturbation Expansion for Surface Scattering. *Radio Sci.* **January/February 1992**, 27 (1), 79–93.
19. Sarabandi, K.; Chiu, T. Electromagnetic Scattering From Slightly Rough Surfaces with Inhomogeneous Dielectric Profiles. *IEEE Trans. Antennas Propagat.* **September 1997**, 45 (9), 1419–1430.
20. Liao, D. H.; Sarabandi, K. On the Effective Low-Grazing Reflection Coefficient of Random Terrain Roughness for Modeling Near-Earth Radiowave Propagation. *IEEE Trans. Antennas Propagat.* **April 2010**, 58 (4), 1315–1324.
21. Warnick, K. F.; Chew, W. C. Numerical Simulation Methods for Rough Surface Scattering. *Waves in Random Complex Med.* **2001**, 11, R1–R30.
22. Liao, D. H.; Michielssen, E.; Sarabndi, K. Simulation of Terrain Propagation and Diffraction Using a 2D High-Order Accurate FMM Accelerated Nyström’s Solver. *IEEE Antennas and Propagat. Soc. Symposium Digest* **2007**, 3740–3743.
23. Liao, D. H.; Sarabandi, K. Simulation of Near-Ground Long Distance Radiowave Propagation Over Terrain Using Nyström Method With Phase Extraction Technique and FMM-Acceleration. *IEEE Trans. Antennas Propagat.* **December 2009**, 57 (12), 3882–3890.
24. Poggio, A. J.; Miller, E. K. Integral Equation Solutions of Three Dimensional Scattering Problems. In R. Mittra, editor, *Computer Techniques for Electromagnetics*. Hemisphere: Washington D.C., 1987.
25. Chang, Y.; Harrington R. F. A Surface Formulation for Characteristic Modes of Material Bodies. *IEEE Trans. Antennas Propagat.* **November 1977**, 25 (6), 789–795.
26. Wu, T. K.; Tsai, L. L. Scattering From Arbitrarily-Shaped Lossy Dielectric Bodies of Revolution. *Radio Sci.* **Ocober1977**, 12 (5), 709–718.
27. Canino, L. F.; Ottusch, J. J.; Stalzer, M. A.; Visher, J. L.; Wandzura, S. M. Numerical Solution of the Helmholtz Equation in 2D and 3D Using a High-Order Nyström Discretization. *J.Comput. Phys.* **1998**, 146.

28. Thorsos, E. I. The Validity of the Kirchhoff Approximation for Rough Surface Scattering Using a Gaussian Roughness Spectrum. *J. Acoust. Soc. Am.* **January 1988**, 83.
29. Ye, H.; Jin, Y.-Q. Parameterization of the Tapered Incident Wave for Numerical Simulation of Electromagnetic Scattering From Rough Surface. *IEEE Trans. Antennas Propagat.* **March 2005**, 53 (3), 1234–1237.
30. Johnson, J. T. A Numerical Study of Low-Grazing Angle Backscatter From Ocean-Like Impedance Surfaces With the Canonical Grid Method. *IEEE Trans. Antennas Propagat.* **January 1998**, 46 (1), 114–120.
31. Johnson, J. T.; Burkholder, R. J.; Toporkov, J. V.; Lyzenga, D. R.; Plant, W. J. A Numerical Study of the Retrieval of Sea Surface Height Profiles From Low Grazing Angle Radar Data. *IEEE Trans. Geosci. Remote Sensing* **January 2009**, 47 (6), 1641–1650.
32. Li, Q.; Chan, C. H.; Tsang, L. Monte Carlo Simulations of Wave Scattering From Lossy Dielectric Random Rough Surfaces Using the Physics-Based Two-Grid Method and the Canonical-Grid method,” *IEEE Trans. Antennas Propagat.* **April 1999**, 47 (4), 752–763.
33. Chan, C. H.; Tsang, L. Monte Carlo Simulations of Large-Scale One-Dimensional Random Rough-Surface Scattering at Near-Grazing Incidence: Penetrable Case. *IEEE Trans. Antennas Propagat.* **January 1998**, 46 (1), 142–149.
34. Oh, Y.; Sarabandi, K. Improved Numerical Simulation of Electromagnetic Wave Scattering From Perfectly Conducting Random Surfaces. *Proc. Inst. Elect. Eng.-Microwave Antennas Propagat.* **August 1997**, 144, 256–260.
35. Zhao, Z.; West, J. C. Resistive Suppression of Edge Effects in MLFMA Scattering From Finite Conductivity Surfaces. *IEEE Trans. Antennas Propagat.* **May 2005**, 53 (5), 1848–1852.
36. Spiga, P.; Spriano, G.; Saillard, M. Scattering of Electromagnetic Waves From Rough Surfaces: A Boundary Integral Method for Low-Grazing Angles. *IEEE Trans. Antennas Propagat.* **July 2008**, 56 (7), 2043–2050.
37. Dogaru, T.; Collins, L.; Carin, L. Optimal Time-Domain Detection of a Deterministic Target Buried Under a Randomly Rough Interface. *IEEE Trans. Antennas Propagat* **March 2001**, 49, 313–326.
38. Taflove, A.; Hagness, S. C. *Computational Electrodynamics: The Finite-Difference Time Domain Method, Third Edition*. Artech House: Boston, MA. 2005.
39. Hastings, F. D.; Schneider, J. B.; Broschat, S. L. A Monte-Carlo FDTD Technique for Rough Surface Scattering. *IEEE Trans. Antennas Propagat.* **November 1995**, 43 (11), 1183–1191.

40. Rabus, B.; When, H.; Nolan, M. The Importance of Soil Moisture and Soil Structure for InSAR Phase and Backscatter, as Determined by FDTD Modeling. *IEEE Trans. Geosci. Remote Sensing* **May 2010**, 48 (5), 2421–2429.
41. Li J.; Guo, L.-X.; Zeng, H. FDTD Investigation on Electromagnetic Scattering From Two-Layered Rough Surfaces under UPML Absorbing Condition. *Chin. Phys. Lett.* **2009**, 26 (2).
42. Hubral, P.; Tygel, M. Analysis of the Rayleigh Pulse. *Geophysics* **1989**, 54, 654–658.
43. Knab, J. J. Interpolation of Band-Limited Functions Using the Approximate Prolate Series. *IEEE Trans. Info. Theory* **November 1979**, 25 (6), 717–720.
44. Li, S.-Q.; Chan, C. H.; Tsang, L.; Li, Q.; Zhou, L. Parallel Implementation of the Sparse-Matrix/Canonical grid Method for the Analysis of Two-Dimensional Random Rough Surfaces (Three-Dimensional Scattering Problem) on a Beowulf System. *IEEE Trans. Geosci. Remote Sensing* **July 2000**, 38 (4), 1600–1608.
45. Xu, P.; Tsang, L. Rough Surface Effects in Microwave Remote Sensing: Numerical Maxwell Model Using the UV/SMCG Method. *IEEE Geosci. Remote Sensing. Symposium Digest* **July 2005**, 2207–2210.
46. Xu, P.; Tsang, L. Scattering of Waves by Rough Surface Based on a Hybrid UV/SMCG Method. *IEEE Antennas and Propagat. Soc. Symposium Digest* **July 2005**, 450–453.
47. Jandhyala, V.; Michielssen, E.; Balasubramaniam, S.; Chew, W. C. A Combined Steepest Descent-Fast Multipole Algorithm for the Fast Analysis of Three-Dimensional Scattering by Rough Surfaces. *IEEE Trans. Geosci. Remote Sensing* **May 1998**, 36 (3), 738–748.
48. Torrungrueng, D.; Johnson, J. T. An Improved FB/NSA Algorithm for the Computation of Scattering From Two-Dimensional Large-Scale Rough Surfaces. *J. of Electromagn. Waves and Appl.* **2001**, 15 (10), 1337–1362.
49. Fung, A. K.; Shah, M. R.; Tjuatja, S. Numerical Simulation of Scattering From Three-Dimensional Randomly Rough Surfaces. *IEEE Trans. Geosci. Remote Sensing* **September 1994**, 32 (5), 986–994.
50. Kuang, L.; Jin Y.-Q. Bistatic Scattering From a Three-Dimensional Object Over a Randomly Rough Surface Using the FDTD Algorithm. *IEEE Trans. Antennas Propagat.* **August 2007**, 55 (8), 2302–2311.
51. Guo, L.-X.; Li, J.; Zeng, H. Bistatic Scattering From a Three-Dimensional Object Above a Two-Dimensional Randomly Rough Surface Modeled with the Parallel FDTD Approach. *J. Opt. Soc. Am. A* **November 2009**, 26 (11), 2383–2392.
52. Dogaru, T. *AFDTD User's Manual*; ARL-TR-5145; U.S. Army Research Laboratory: Adelphi, MD, Mar. 2010.

53. Zhu, X.; Carin, L.; Dogaru, T. Parallel Implementation of the Biorthogonal Multiresolution Time-Domain Method. *J. Opt. Soc. Am. A* **May 2003**, 20 (5), 844–855.
54. Macelloni, G.; Nesti, G.; Pampaloni, P.; Sigismondi, S.; Tarchi, D.; Lolli, S. Experimental Validation of Surface Scattering and Emission Models. *IEEE Trans. Geosci. Remote Sensing* **January 2000**, 38 (1), 459–469.
55. Borcea, L.; Papanicolaou, G.; Tsogka, C. A Resolution Study for Imaging and Time Reversal in Random Media,” *Cont. Mathem.* **2003**, 313, 63–67.
56. Sarabandi, K.; Koh, I.; Casciato, M. D. Demonstration of Time Reversal Methods in a Multi-Path Environment. *IEEE Antennas and Propagat. Soc. Symposium Digest* **June 2004**, 4436–4439.
57. Sullivan, A. *Electromagnetic Modeling and Performance Prediction of Ground-Based Forward-Looking Radar for Improvised Explosive Device (IED) Detection*; ARL-TR-4806; U.S. Army Research Laboratory: Adelphi, MD, May 2009.
58. De Roo, R. D.; Ulaby, F. T.; El-Rouby, A. E.; Nashashibi, A.Y. MMW Radar Scattering Statistics of Terrain at Near-Grazing Incidence. *IEEE Trans. Aerospace Electron. Sys.* **July 1999**, 35 (3), 1010–1018.
59. Abdi, A.; Kaveh, M. K Distribution: An Appropriate Substitute for Rayleigh-lognormal Distribution in Fading-Shadowing Wireless Channels. *Electron. Lett.* **April 1998**, 34 (9), 851–852.
60. Jao, J. K. Amplitude Distribution of Composite Terrain Radar Clutter and the K-Distribution. *IEEE Trans. Antennas Propagat* **October 1984**, 32 (10), 1049–1062.
61. Oliver, C. J. A Model for Non-Rayleigh Scattering Statistics. In B.J. Uscinski, editor, *Wave Propagation and Scattering*. Clarendon: Oxford, 1986.
62. Dong, Y. *Models of Land Clutter vs. Grazing Angle, Spatial Distribution, and Temporal Distribution—L-Band VV Polarisation Perspective*, Research Report, DSTO-RR-0273, DSTO, 2004.
63. Long, M. W. *Radar Reflectivity of Land and Sea*. Artech House: Dedham, MA., 1983.
64. Nassar, E. M.; Johnson, J. T. A Numerical Model for Electromagnetic Scattering From Sea Ice. *IEEE Trans. Geosci. Remote Sensing* **May 2000**, 38 (3), 1309–1319.

---

## List of Symbols, Abbreviations, and Acronyms

---

APSWF	approximate prolate spheroidal wave function
ARL	U.S. Army Research Laboratory
CPU	central processing unit
DSRC	DoD Supercomputing Resource Center
FDTD	finite-difference time-domain
FMM	fast multipole method
<i>hh</i>	horizontal-horizontal
<i>hv</i>	horizontal-vertical
KA	Kirchhoff approximation
LCN	locally corrected Nyström
MoM	method of moments
MPI	Message-Passing Interface
PMCHWT	Poggio, Miller, Chang, Harrington, Wu, and Tsai
PML	perfectly matched layer
RCS	radar cross section
<i>rms</i>	root mean square
SDFMM	steepest descent-fast multipole method
SIE	surface integral equation
SIRE	synchronous impulse reconstruction
SPM	small perturbation method
TF/SF	total field/scattered field
UHF	ultra high frequency
UXO	unexploded ordnances
<i>vh</i>	vertical-horizontal

VHF	very high frequency
vv	vertical-vertical

NO. OF COPIES	ORGANIZATION
1	ADMNSTR DEFNS TECHL INFO CTR ATTN DTIC OCP 8725 JOHN J KINGMAN RD STE 0944 FT BELVOIR VA 22060-6218
11	US ARMY RSRCH LAB ATTN IMNE ALC HRR MAIL & RECORDS MGMT ATTN RDRL CIO LL TECHL LIB ATTN RDRL CIO MT TECHL PUB ATTN RDRL SER U TRAIAN DOGARU KARL KAPPRA CHRIS KENYON CALVIN LE DAHAN LIAO (3 COPIES) ANDY SULLIVAN ADELPHI MD 20783-1197